A muographic study of a scoria cone from 11 directions using nuclear emulsion cloud chambers

Seigo Miyamoto[1], Shogo Nagahara[1,2], Kunihiro Morishima[3], Toshiyuki Nakano[3], Masato Koyama[4], Yusuke Suzuki[5]

[1]Earthquake Research Institute, The University of Tokyo, 1-1-1 Yayoi, Bunkyo-ku, Tokyo, 113-0032, Japan.
[2]Graduate School of Human Development and Environment, Kobe University, 3-11 Tsurukabuto, Nada-ku, Kobe, Hyogo, 657-8501, Japan.
[3]Fundamental Particle Physics Laboratory, Graduate School of Science of Nagoya University, Furocho, Chikusa-ku, Nagoya, Aichi, 464-8602, Japan.
[4]Center for Integrated Research and Education of Natural Hazards, Shizuoka University, 836 Oya, Suruga-ku, Shizuoka City, Shizuoka, Japan.
[5]STORY, Ltd., 2-2-5-2321, Minatomachi, Naniwa-ku, Osaka City, Osaka, Japan.

Correspondence to: Seigo Miyamoto (miyamoto@eri.u-tokyo.ac.jp)

Abstract

One of the key challenges for muographic studies is to reveal the detailed 3D density structure of a volcano by increasing the number of observation directions. 3D density imaging by multi-directional muography requires that the individual differences in the performance of the installed muon detectors are small and that the results from each detector can be derived without any bias in the data analysis. Here we describe a pilot muographic study of the Izu–Omuroyama scoria cone in Shizuoka Prefecture, Japan, from 11 directions, using a new nuclear emulsion detector design optimized for quick installation in the field. We describe the details of the data analysis and present a validation of the results.

The Izu–Omuroyama scoria cone is an ideal target for the first multi-directional muographic study, given its expected internal density structure and the topography around the cone. We optimized the design of the nuclear emulsion detector for rapid installation at multiple observation sites in the field, and installed these at 11 sites around the volcano. The images in the developed emulsion films were digitized into segmented tracks with a high-speed automated readout system. The muon tracks in each emulsion detector were then reconstructed. After the track selection, including straightness filtering, the detection efficiency of the muons was estimated. Finally, the density distributions in 2D angular space were derived for each observation site by using a muon flux and attenuation models.

The observed muon flux was compared with the expected value in the free sky, and is 88% ± 4% in the forward direction and 92% ± 2% in the backward direction. The density values were validated by comparison with the values obtained from gravity measurements, and are broadly consistent, except for one site. The excess density at

41 this one site may indicate that the density inside the cone is non-axisymmetric, which
42 is consistent with a previous geological study.

43 **1 Introduction**

44 Scoria or cinder cones are a simple volcanic structure, along with stratovolcanoes,
45 shield volcanoes, and lava domes. Understanding the internal structure of scoria cones
46 is important for volcanic hazard assessments. The internal structure of scoria cones
47 has been mainly investigated by geological approaches. Kereszturi and Németh (2012)
48 presented a schematic cross-section of typical scoria cones, and Geshi and Neri (2014)
49 presented detailed photographs of the feeder dike and interior of a scoria cone formed
50 by the 1809 Etna eruption. Yamamoto (2003) investigated outcrops of the interior of
51 scoria cones in the Ojika-jima monogenetic volcano group, Nagasaki Prefecture, Japan.
52 Yamamoto (2003) classified 40 scoria cones according to their degree of interior welding
53 and proposed a link between lava outflow and cone collapse. However, scoria cones with
54 such outcrops are rare, and the internal structure can vary markedly among cones.
55 Therefore, non-destructive methods are required to investigate scoria cones that lack
56 outcrops.
57 Muography is a non-destructive technique for investigating the internal density
58 structure of large objects, employing the strong penetrating force of muons, which are
59 high-energy elementary particles contained in cosmic rays. Muography has also been
60 used for studying volcanoes, including visualization of a shallow conduit (e.g., Tanaka
61 et al., 2009), detection of temporal changes in water level due to hydrothermal activity
62 (Jourde et al., 2016), and 3D density imaging of a lava dome using a joint inversion of
63 muographic and gravity data (Nishiyama et al., 2017).

In unidirectional muography, the only measurable quantity is the density length, which is the integral of density and length along the muon direction. It has no spatial resolution along the muon path. Therefore, even if an interesting density contrast is found below the crater, this could reflect contributions from other parts of the volcanic body. Similar to X-ray computed tomography, which has been developed as a 3D density imaging technique, muography can obtain 3D spatial resolution by increasing the number of observation directions. In previous studies, muography of volcanoes has been conducted in two or three directions (Tanaka et al., 2010; Rosas-Carbajal et al., 2017). However, the spatial resolution is not sufficient to determine the detailed structure of the volcanic interior. Nagahara and Miyamoto (2018) undertook a 3D density reconstruction based on multi-directional muography and the filtered back-projection technique. Their study showed that it is necessary to increase the number of directions to obtain 3D spatial resolution in volcanological studies.

Nuclear emulsion is a type of muon detector, and has been used for studies of volcanoes (Tanaka et al., 2007; Nishiyama et al., 2014; Tioukov et al., 2019). The trajectories of high-energy charged particles that pass through an emulsion film are recorded as aligned silver grains with micron-scale resolution (Nakamura et al., 2005; Tioukov et al., 2019; Nishio et al., 2020). The positions and slopes of aligned grains in a developed emulsion film are digitized with an automated emulsion readout system (Kreslo et al., 2008; Morishima and Nakano, 2010; Bozza et al., 2012; Yoshimoto et al., 2017). Unlike hodoscopes using scintillator bars (e.g., Saracino et al., 2017) or multi-wire proportional chambers (Olah et al., 2018), a nuclear emulsion film does not have temporal resolution. In contrast, an emulsion detector does not require electricity,

87 which facilitates the installation of such detectors around volcanoes where the
88 infrastructure is not well developed.
89 In muographic studies of a volcano, contamination by low-momentum particles must
90 be removed to derive the correct density (Nishiyama et al., 2014, 2016). Thus, nuclear
91 emulsion detectors have often been used as an emulsion cloud chamber (ECC), which
92 comprises alternating layers of films and lead or iron plates (e.g., Kodama et al., 2003).
93 An ECC detector can measure the momentum of the charged particles, one by one, by
94 detecting deflection angles caused by multiple Coulomb scattering (Agafonova et al.,
95 2012). For multiple Coulomb scattering, there is a relationship between the maximum
96 detectable momentum p_{max} and position resolution y_{reso} as follows using the first term
97 of Eq. (33.16), and (33.20) in Tanahashi et al., (2018):
98 $$p_{max} \sim \alpha\, X_0^{-0.5}\, x^{1.5}\, y_{reso}^{-1} \qquad (1)$$
99 where α is a constant, X_0 is the radiation length of a material, and x is the thickness of
100 the material. The position resolution of the newest scintillator hodoscope or MWPC is
101 on the order of 1 mm (Saracino et al., 2017; Olah et al., 2018). In the case of nuclear
102 emulsion, the resolution is about 1 μm. When using ECC, the thickness of the material
103 can be reduced to 1/100 while maintaining the same p_{max}, which is advantageous in
104 terms of transportation in the field.
105 A new design of the ECC detector was also required for its rapid installation at
106 multiple observation sites in the field. In a previous study of volcano observations
107 using the ECC detector (Nishiyama et al., 2014), rapid installation of the detector was
108 not required because the number of observation sites was just one. It is also important
109 to establish a data analysis procedure for the muon tracks recorded by the ECC
110 detectors. To derive an accurate density value for the volcanic body, it is necessary to

111 remove low-momentum contamination, estimate the detection efficiency, and validate
112 the results. In addition, for bias-free 3D imaging by multi-directional muography, the
113 installed muon detectors must show similar performance.

114 **2 Izu–Omuroyama scoria cone**

115 The Izu–Omuroyama scoria cone (34°54'11"N, 139°05'40"E; 580 m a.s.l.) is one of the
116 largest scoria cones in the world, and is part of the Higashi Izu monogenetic volcano
117 group (Aramaki and Hamuro, 1977), which is located in the northeastern Izu
118 Peninsula, Ito City, Shizuoka Prefecture, Japan. It is considered to have formed about
119 4,000 years ago, based on ^{14}C dating (Saito et al., 2003). The basal diameter is 1,000 m,
120 the height is 280 m from the base, and the typical slope of its flanks are 29–32°. The
121 center of the cone contains a crater that is 250 m wide and 40 m deep. The volume of
122 the cone is 71×10^6 m^3, and lava with a volume of $\sim 10^8$ m^3 has flowed out from the
123 base of the cone (Koyano et al., 1996). The lava is a basaltic andesite with 54–56 wt.%
124 SiO_2 (Hamuro, 1985).
125 Although the shape of the Izu–Omuroyama scoria cone appears to be axisymmetric
126 (Fig. 1), a geological study suggested it has an anisotropic structure due to the
127 following reasons. (i) During/after the growth of the cone, some interior parts became
128 welded due to loading, residual heat, and a low cooling rate. As a result, some denser
129 material formed. (ii) At the end of the eruption, a lava lake was formed in the crater,
130 and the lava flowed out to the western foot of the cone. (iii) There is a small crater on
131 the south side of the cone, which is thought to have formed when the main crater was
132 blocked at the end of the eruption (Koyano et al., 1996).

The bulk density of typical continental crust is about 2.6–2.7 × 10^3 kg m^{-3}. The bulk densities reported for scoria deposits are 0.84–1.01 × 10^3 kg m^{-3} (Taha and Mohamed, 2013) and 0.56–1.20 × 10^3 kg m^{-3} (Bush, 2001). Therefore, the maximum expected density contrast is about 1.4–2.0 × 10^3 kg m^{-3}, due to the difference in porosity between welded rocks and scoria deposits. In addition, the Izu–Omuroyama scoria cone is an ideal target for multi-directional muography due to the accessibility to detector sites and absence of muographic shadows from any direction caused by other topographic features.

142

143

144

145 Figure 1. Photograph of the Izu–Omuroyama scoria cone from the northwest, taken by

146 an unmanned aerial vehicle (Koyama, 2017).

147

3 Multi-directional muography observations using emulsion cloud chambers

3.1 Detector design

Emulsion films were manufactured by pouring 70 μm of nuclear emulsion on both sides of a 180 μm-thick plastic base. The size of a film is 125 × 100 mm. The films were vacuum-packed in a light-blocking envelope to maintain their planar form, which prevented air bubbles forming between the envelope and film, and made it easy to handle the films in the field.

The detector used for the 2018 observations is basically the same as that of Nishiyama et al. (2014), and only the number of lead plates was different. The former consists of 20 films and 9 plates of 1-mm-thick lead, the latter consists of 20 films and 19 lead plates. At the time of installation in 2018, the films, lead plates, and supports were all in pieces and, therefore, a lot of time and effort was required for assembly in the field. The more efficient detector design was required for rapid and error-free installation.

The detector used in the 2019 observations was improved. It consists of an ECC and an outer box. The ECC consists of 20 emulsion films and 19 lead plates, each 1 mm thick (Fig. 2a). An aluminum frame was fixed to a lead plate with a thin sheet of glue, and then an emulsion film with the light-blocking envelope was attached with scotch tape. In this paper, we term this unit the emulsion–lead plate (EL plate; Fig. 2a). The EL plate was designed for quick assembly in the field.

The outer box consists of 10-mm-thick aluminum plates (Fig. 2b). The outer size of this box is 190 mm in width, 155 mm in height, and 90 mm in depth. An ECC and strong springs were placed in the box. There are four screw holes on one side of the box, and by turning the bolts and pushing the spring plate, a uniform pressure (~10^5 Pa)

171 was applied to the ECC. This pressure prevents the film from stretching and shrinking
172 due to temperature changes.
173 Given that there is no temporal resolution in emulsion films, ordinary ECC detectors
174 cannot distinguish whether cosmic-ray tracks pass the ECC during muographic
175 observation or transportation and standby. Thus, we also added a similar gimmick as
176 previous muographic studies using emulsion films as previous muographic studies
177 using emulsion films. The researchers have been used emulsion films with a different
178 alignment during the muon observations and standby (e.g., Tanaka et al., 2007). In the
179 present study, the corners of the EL plates were aligned during the muon observations,
180 while the corners were intentionally shifted a few millimeters horizontally and fixed
181 with clamps during standby (Fig. 3). This alignment difference distinguishes passing
182 charged particles during non-observation and observation periods by pattern matching
183 of each emulsion film. By using this procedure, the time to set the alignment between
184 each EL plate in the field is <30 s. Although the muon tracks that pass through an
185 ECC during the alignment set-up may become noise, our procedure reduced such
186 tracks.
187

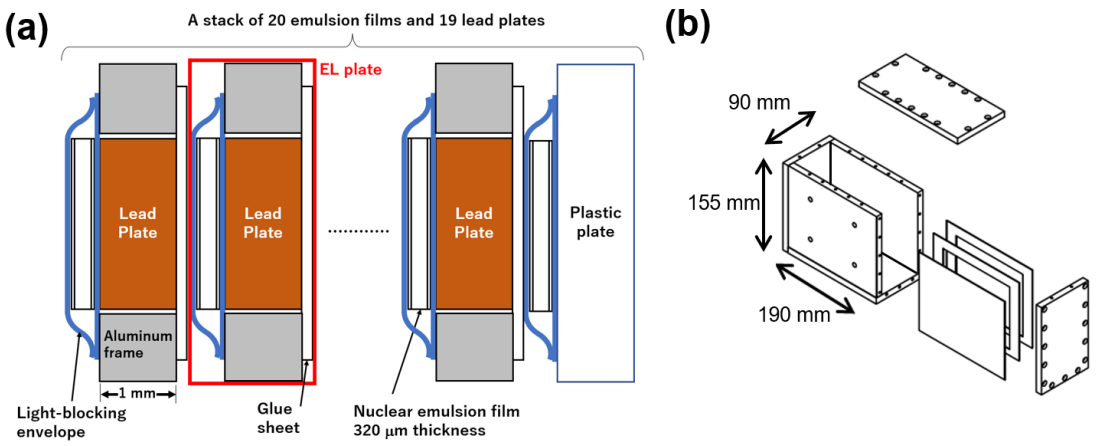

188

189 Figure 2. Design of the ECC and outer box. (a) Schematic cross-section of the EL plates
190 and an ECC. The EL plate consists of a 1-mm-thick aluminum frame, 1-mm-thick lead
191 plate, 100-μm-thick glue sheet that fixes a lead plate to an aluminum frame, and an
192 emulsion film with a light-blocking envelope. An ECC consists of 19 EL plates and an
193 emulsion film with a plastic plate. (b) Schematic of the aluminum outer box. The
194 thickness of the aluminum plate is 10 mm. The ECC shown in (a) was set inside this
195 box. There are four holes for feed screws in the front plate.

196

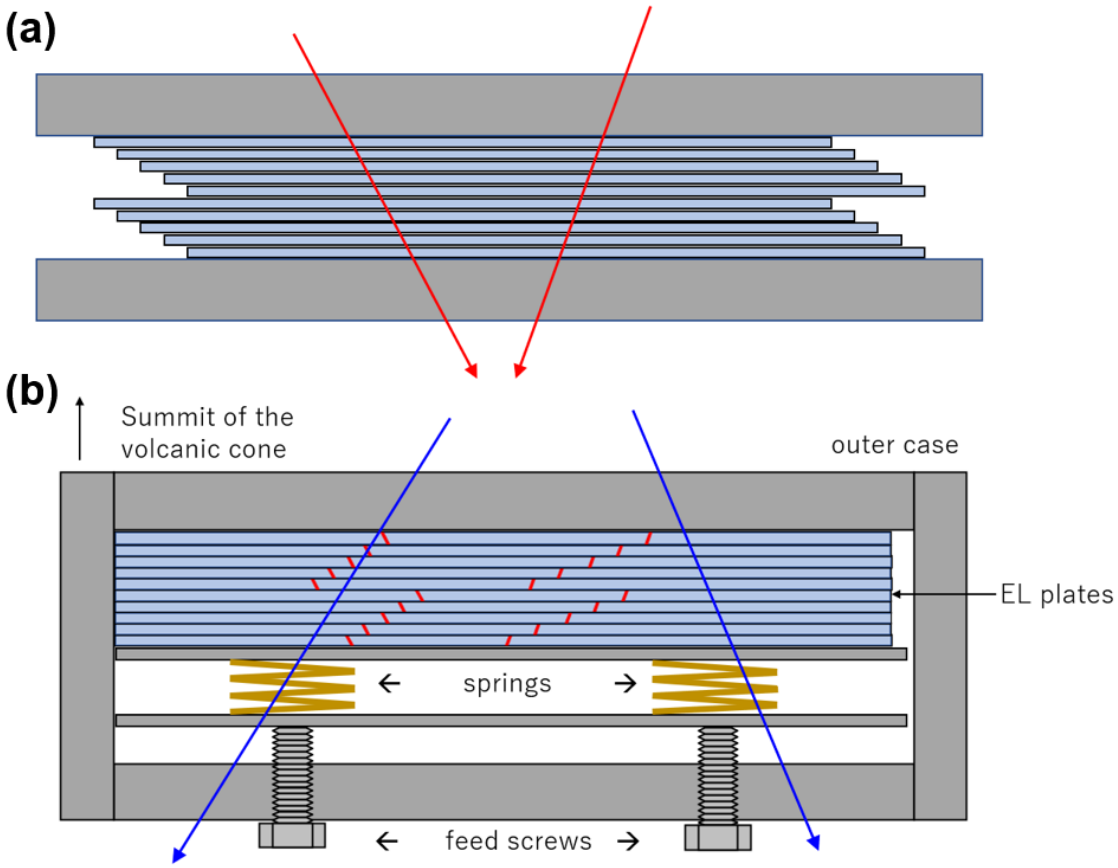

Figure 3. (a) View of the EL plates from above during standby. The EL plates were intentionally shifted a few millimeters horizontally and fixed with a pair of steel plates and clamp. The red lines represent the muon tracks in this alignment. (b) View from above during the observations. The EL plates were aligned to the side of the outer box, and fixed by the springs and feed screws. The blue lines represent muon tracks during observations. Note that the red tracks cannot be reconstructed in this alignment.

3.2 Installation

The detectors were installed at three sites in 2018 and eight sites in 2019 around the Izu–Omuroyama scoria cone (Fig. 4; Table 1). Each detector was buried in a hole that was about 40 cm deep to avoid high temperatures due to direct sunlight. This is done because the number of latent image specks decreases, and the number of randomly generated specks increases, under high-temperature conditions (Nishio et al., 2020).

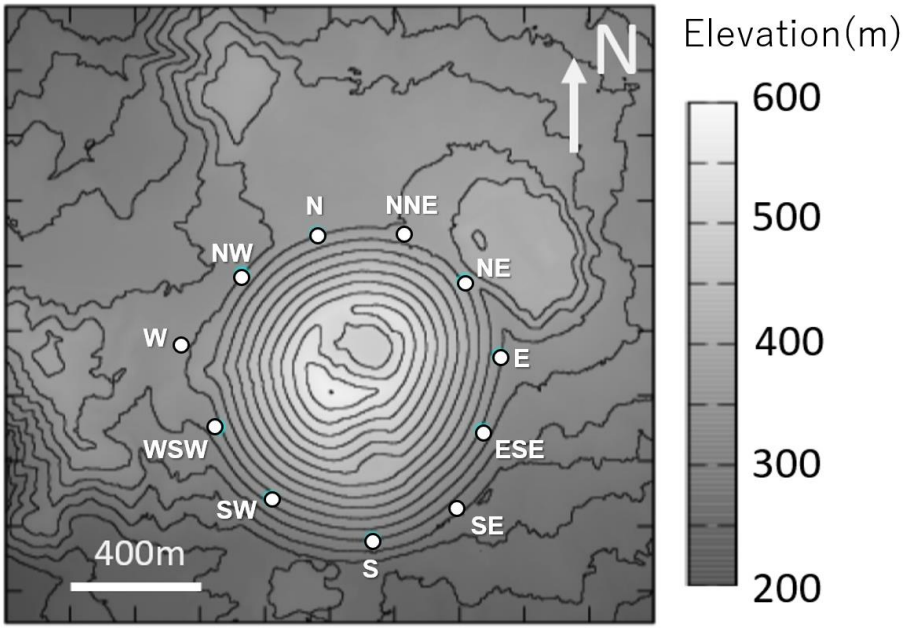

Figure 4. Topography of the Izu–Omuroyama scoria cone. White dots represent observation sites.

Detector site ID	Effective area ($\times 10^{-4}$ m^2)	Exposure time (days)
W, SE, and NNE (2018)	120	60
N, NW, WSW, SW, S, ESE, E, and NE (2019)	240	90

Table 1. Effective area and muon exposure time for each detector.

222

223 The installation procedure at each observation site in 2019 was as follows (Fig. 5).

224 1) Carry the outer box and EL plates to the observation site.

225 2) Measure the coordinates of the site with a hand-held GPS (GERMIN; model GPS
226 eTrex 30J). The typical uncertainty of the latitudinal and longitudinal coordinates
227 is 3 m.

228 3) Dig a hole in the ground with horizontal dimensions of 60 × 40 cm and a depth of
229 40 cm.

230 4) Flatten the base of the hole, place a plastic bag inside the hole, and lay down a
231 piece of plywood.

232 5) Put double-sided tape on the bottom of the outer box and place it on the plywood.

233 6) Put the stack of EL plates into the box and quickly align these (<30 s).

234 7) Close the cap of the outer box.

235 8) Turn the feed screws to increase the pressure.

236 9) Measure the attitude of the outer box (i.e., the yaw [absolute azimuth angle], roll,
237 and pitch). The yaw was measured with a fiber optic gyro (Japan Aviation
238 Electronics Industry Ltd.; model FOG JM7711; Watanabe et al., 2000), and the roll
239 and pitch were measured by the digital leveler. The typical errors on the yaw, roll,
240 and pitch are 8.7×10^{-3}, 1.0×10^{-3}, and 1.0×10^{-3} radians, respectively.

241 10) Cover with styrofoam to avoid heating from the ground surface.

242 11) Close the plastic bag to keep water out.

243 12) Backfill the hole.

244

245 The time taken for this installation was ~2 h for each site, and we installed detectors
246 as three sites in a day in 2019. The detector retrieval procedure was the opposite of the
247 installation procedure. The 380 films were developed in a darkroom. The deposited
248 silver particles on the surface of the films were removed with anhydrous ethanol. The
249 gelatin of the sensitive layer was swollen with a glycerin solution to obtain the
250 optimum thickness for an automated track readout system, which is described in the
251 next section.
252

253

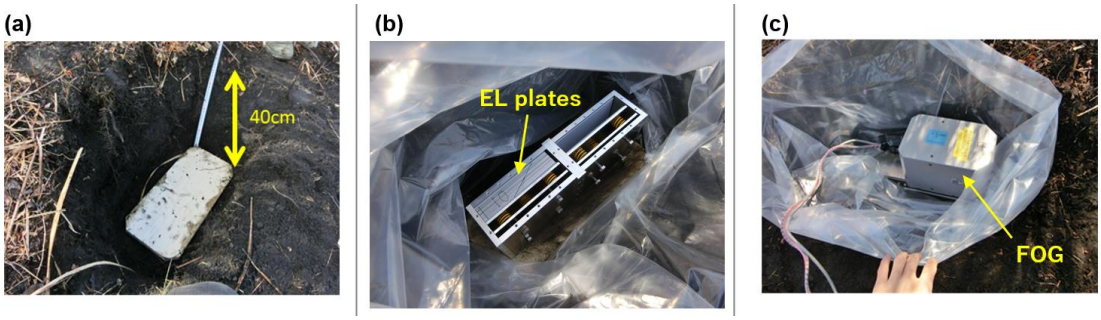

254

255

256 Figure 5. Photographs showing the installation procedure. (a) Dig a hole and place a
257 plywood sheet in the bottom. (b) Place the outer box in the hole and put a stack of EL
258 plates into the box. The plates were aligned over a period of <30 s. After closing the top
259 plate of the box, the feed screws were tightened to increase the pressure. (c) The yaw,
260 roll, and pitch were measured with a fiber optic gyro (FOG) and digital leveler.

261

4 Track reconstruction, selection, and detection efficiency estimation

4.1 Track reconstruction

A track of a high-energy charged particle is recorded as an aligned line of silver grains in the emulsion film (e.g., Nakamura et al., 2005). The images in the 380 nuclear emulsion films were scanned and the positions and slopes of the tracks were digitized by "HTS", which is a high-speed automated track readout system at Nagoya University (Yoshimoto et al., 2017). For each ECC, the tracks of the charged particles were digitally reconstructed from the segmented tracks in 20 films. NETSCAN 2.0 software was used for track reconstruction (Hamada et al., 2012). NETSCAN 2.0 rapidly corrects for film distortions and local misalignments between films by using many tracks recorded over a large area. It then outputs all possible connections as the final result. NETSCAN 2.0 has been used in various fields, such as neutrino physics (Hiramoto et al., 2020), cosmic ray astronomy (Takahashi et al., 2015), and muographic studies of Egyptian pyramids (Morishima et al., 2017). The typical procedure for the track reconstruction is as follows.

1) Reconstruct the "base track", which is connected between the emulsion layers across the plastic base of 170 μm in a film.
2) Reconstruction of the "linklet", which is the base track pair between adjacent films across lead plates.
3) Reconstruction of the tracks that connect across the whole ECC. If no base track was found in two consecutive films on the extension of a track, then the track was considered to have stopped.

For example, in ECC_ID = 02, 8.9 × 10^6 base tracks, 3.2 × 10^6 linklets in a pair of adjacent films, and 1.7 × 10^7 tracks in an entire ECC were reconstructed.

4.2 Track selection

NETSCAN 2.0 outputs all possible track connections. Therefore, it is necessary to carefully select the tracks for the muographic analysis. A schematic example of the output tracks is shown in Fig. 6. Most of the branches can be considered to represent contamination by fake base tracks caused by random noise, or the coincidental occurrence of low-energy positrons/electrons on parallel slopes in the vicinity of the real tracks (e.g., Fig. 6; cases 2 and 3). For reference, the position dependence of noise density is described in Appendix A. Some branches consist of a pair of straight tracks with small closest distances and similar angles (Fig. 6; case 4). In this case, the two tracks should be separated.

The following χ^2/ndf value was calculated for all tracks for the low momentum cut-off:

$$\chi^2/ndf = \sum_m \left[\left(\frac{\Delta\theta_R^m}{\sigma_R^m} \right)^2 + \left(\frac{\Delta\theta_L^m}{\sigma_L^m} \right)^2 \right] / ndf \qquad (2)$$

where ndf is the number of degrees of freedom and m is the index of adjacent film pairs (i.e., [1,2], [2,3], [3,4], …, and [18,19], [19,20] in Fig. 6) or with one skip if there was a base track inefficiency (i.e., [1,3], [2,4], [3,5], …, [17,19], [18,20]). $\Delta\theta_R^m = (\Delta\theta_x^m \times \tan\theta_x + \Delta\theta_y^m \times \tan\theta_y)/\sqrt{\tan^2\theta_x + \tan^2\theta_y}$ and $\Delta\theta_L^m = (\Delta\theta_y^m \times \tan\theta_x - \Delta\theta_x^m \times \tan\theta_y)/\sqrt{\tan^2\theta_x + \tan^2\theta_y}$, and $\Delta\theta_x^m$ and $\Delta\theta_y^m$ are angular differences along the x, y coordinates of the ECC. σ_R^m and σ_L^m are the root-mean-square of $\Delta\theta_R^m$ and $\Delta\theta_L^m$,

307 which were calculated for every adjacent film pair in every ECC (Fig. 7). Figure 8
308 shows the distribution of χ^2/ndf for all tracks in an ECC.
309 The procedure for track selection is as follows.
310 1) Select tracks that start from one of the two most upstream (i.e., summit cone side)
311 films and stop at one of the two most downstream films.
312 2) Select tracks with $\chi^2/ndf < 5.0$.
313 3) If a track has any branches, then:
314 a) If the shared proportion of track length is ≥20%, choose the longest branch. If
315 the track lengths are the same, then choose the branch with the smallest
316 χ^2/ndf.
317 b) If the shared proportion of track length is <20% (Fig. 6; case 4), then the
318 branches were divided into two tracks.
319 We estimated the effect of the straightness filtering using $\chi^2/ndf < 5.0$. Figure 9 shows
320 the momentum filtering efficiency. This figure was derived from a simple simulation in
321 which the interaction of charged particles inside the ECC was assumed to be multiple
322 Coulomb scattering only, and the scattering angle was approximated by a Gaussian
323 distribution. The path length in the lead plates becomes longer when the track has a
324 larger slope, and thus the momentum also becomes higher. Based on the background
325 noise study by Nishiyama et al. (2016), the size of the mountain body used in the
326 simulation and the Izu–Omuroyama scoria cone is broadly the same, and thus the
327 rejection efficiency should be sufficient. For example, after the track selection,
328 1.7×10^6 tracks were selected at the site "N".
329
330

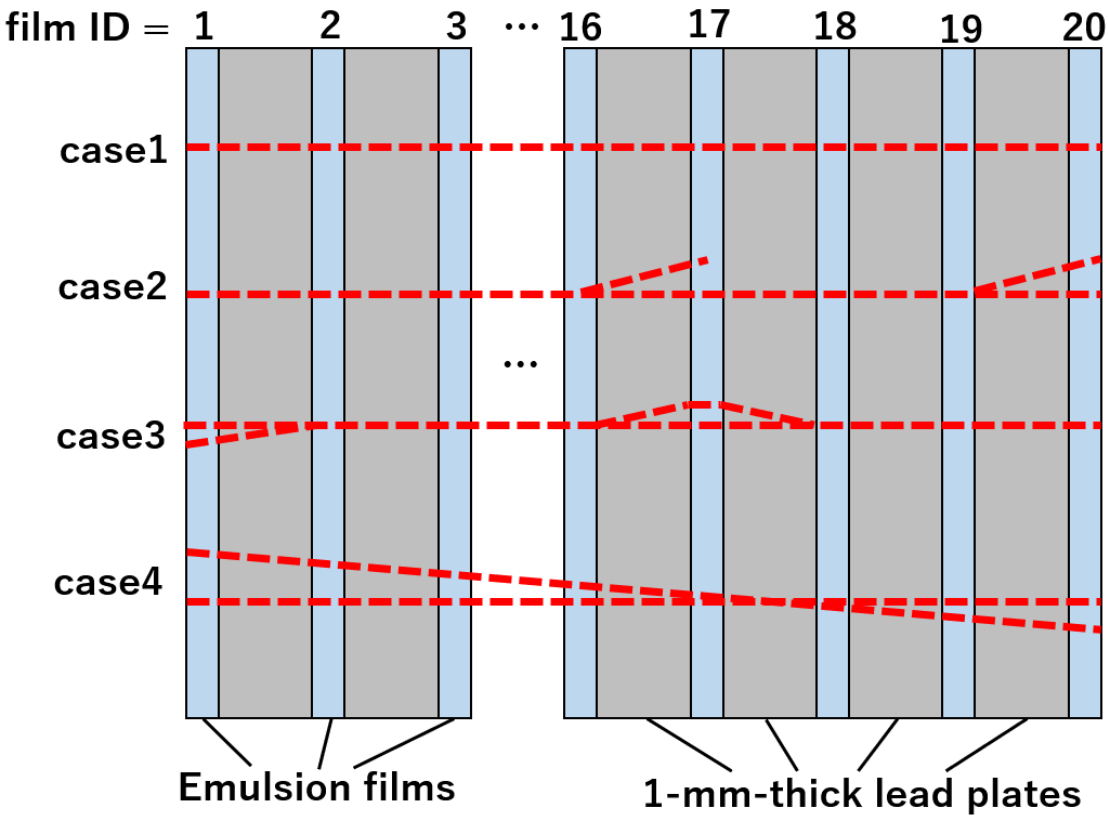

Figure 6. Schematic examples of typical reconstructed tracks in an ECC obtained by NETSCAN 2.0. Upstream means towards the volcanic cone side and downstream means the backward free sky direction.

Case 1: a straight track without any branches.

Case 2: a straight track with a branch in the middle and downstream films. The track branch in the middle was rejected by selection step (1). The branch in the most downstream film was merged into the straight track by selection step 3a.

Case 3: branches in the upstream and middle films. Both branches were merged into a straight track by selection step 3a.

Case 4: a pair of straight tracks with small closest distances and similar angles. If the

344 shared proportion of the track length was <20%, the tracks were divided into two

345 different tracks by selection step 3b.

346

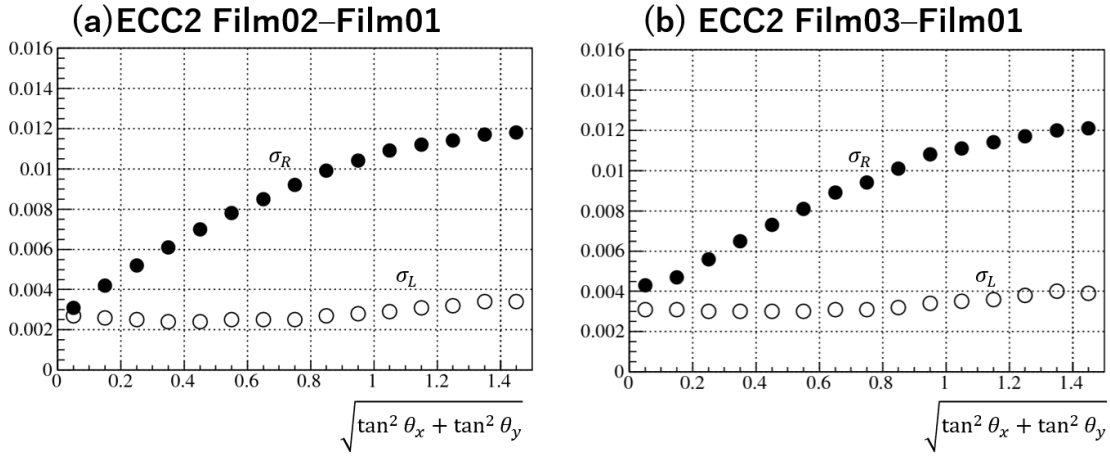

347

348 Figure 7. Examples of σ_R and σ_L as a function of $\sqrt{\tan^2\theta_x + \tan^2\theta_y}$. The values were

349 determined by the ECC and used to calculate the value of Eq. (2).

350

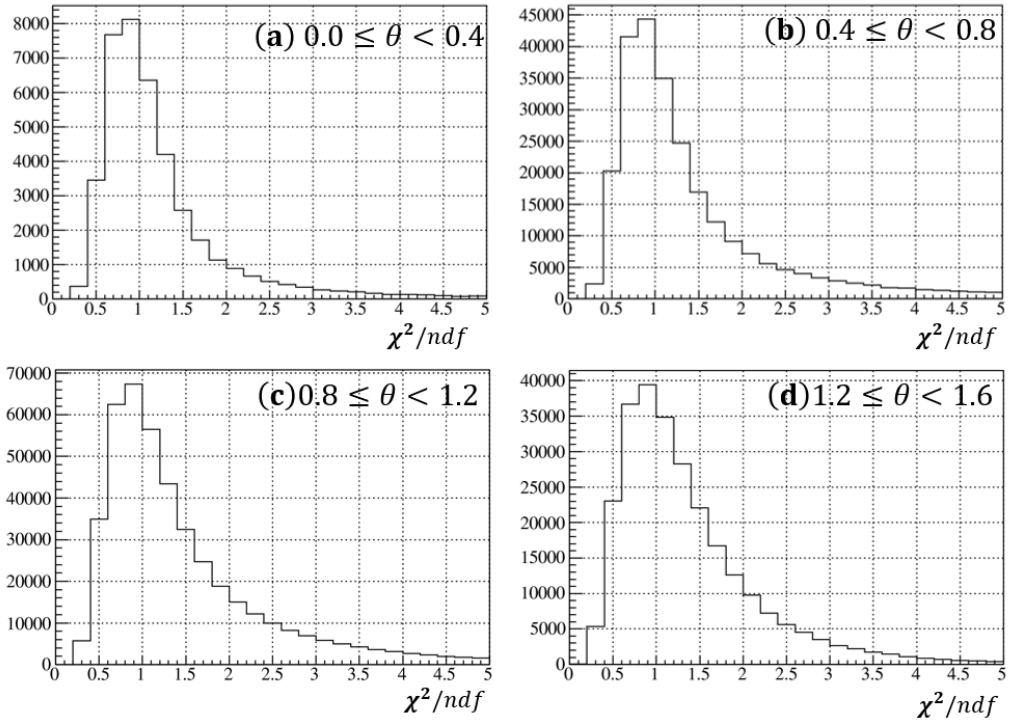

351

352 Figure 8. Example of the χ^2/ndf distribution for selected tracks as a function of $\theta =$

353 $\sqrt{\tan^2\theta_x + \tan^2\theta_y}$ in an ECC. (a) $0 \leq \theta < 0.4$, (b) $0.4 \leq \theta < 0.8$, (c) $0.8 \leq \theta < 1.2$, and (d)

354 $1.2 \leq \theta < 1.6$.

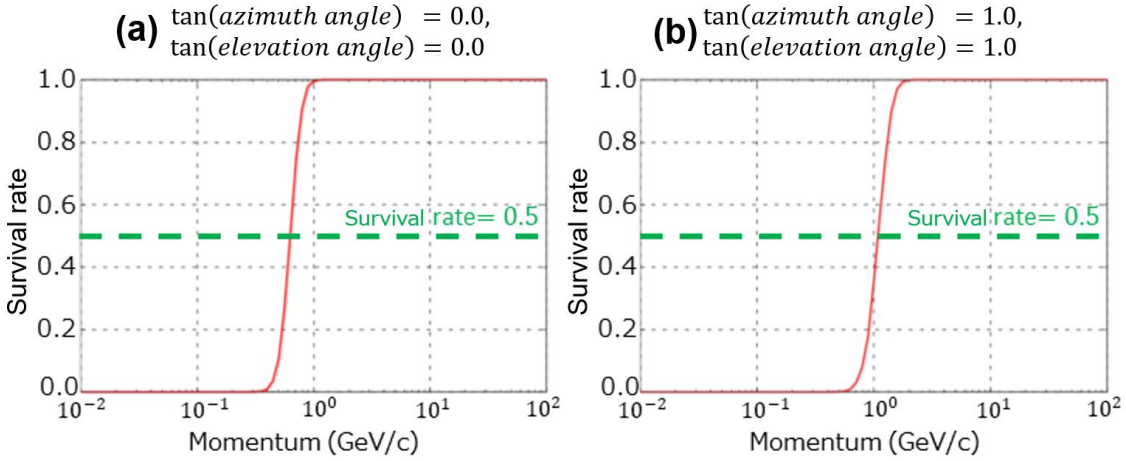

355

356 Figure 9. Survival rate of muons after the straightness cut-off as a function of

357 momentum. (a) Track angles with tan(*relative azimuth*) = 0.0 and

358 tan(*elevation angle*) = 0.0. (b) Track angles with tan(*relative azimuth*) = 1.0 and

359 tan(*elevation angle*) = 1.0. The path length in the lead plates becomes longer when the

360 track has a larger slope, and thus the remaining momentum also becomes higher for

361 the latter case. The momentum values at a survival rate of 0.5 are 0.6 and 1.1 GeV/c,

362 respectively.

363

4.3 Detection efficiency estimation

The muon detection efficiency can be estimated by investigating the percentage of tracks that have a base track in a film. In this paper, we term this percentage the "fill factor". The fill factor ε can be defined as follows:

$$\varepsilon_j(\theta_x, \theta_y) = \frac{N_j(\theta_x, \theta_y)}{N_{j-1,j+1}(\theta_x, \theta_y)} \quad (3)$$

where j is a film ID, $N_{j-1,j+1}(\theta_x, \theta_y)$ is the number of tracks in which base tracks were found in films $j-1$ and $j+1$, and $N_j(\theta_x, \theta_y)$ is the number of tracks in which base tracks were found in films $j-1$, j, and $j+1$. The fill factor depends on the films and track slopes θ_x and θ_y. The position dependence of the fill factor is described in Appendix A.

Using the fill factor $\varepsilon_j(\theta_x, \theta_y)$ and $\bar{\varepsilon}_j(\theta_x, \theta_y) = 1 - \varepsilon_j(\theta_x, \theta_y)$, the muon detection efficiency ϵ in an ECC can be calculated as follows:

$$\epsilon(\theta_x, \theta_y) = \sum_{hit\ pattern} \varepsilon_1 \times \bar{\varepsilon}_2 \times \varepsilon_3 \times \ldots \times \bar{\varepsilon}_{18} \times \varepsilon_{19} \times \varepsilon_{20} \quad (4)$$

where $hit\ pattern$ is the summation for all possible hit patterns (e.g., $\varepsilon_1 \times \bar{\varepsilon}_2 \times \varepsilon_3 \times \ldots \times \bar{\varepsilon}_{18} \times \varepsilon_{19} \times \varepsilon_{20}$ or $\bar{\varepsilon}_1 \times \varepsilon_2 \times \varepsilon_3 \times \ldots \times \varepsilon_{18} \times \bar{\varepsilon}_{19} \times \varepsilon_{20}$) from the track selection conditions described in section 4.2 (Fig. 10). An example of the angular distribution of the fill factor $\varepsilon_j(\theta_x, \theta_y)$ and muon detection efficiency $\epsilon(\theta_x, \theta_y)$ in an ECC is shown in Fig. 11. The statistics of observed muons were limited in some angular bins by the thick volcanic cone. However, the statistics were sufficient in the backward region (i.e., elevation angle < 0.0). We used the distribution of the negative elevation angular region instead of the positive region, because it has enough statistics and the optics of the HTS has an approximately two-fold rotational symmetry.

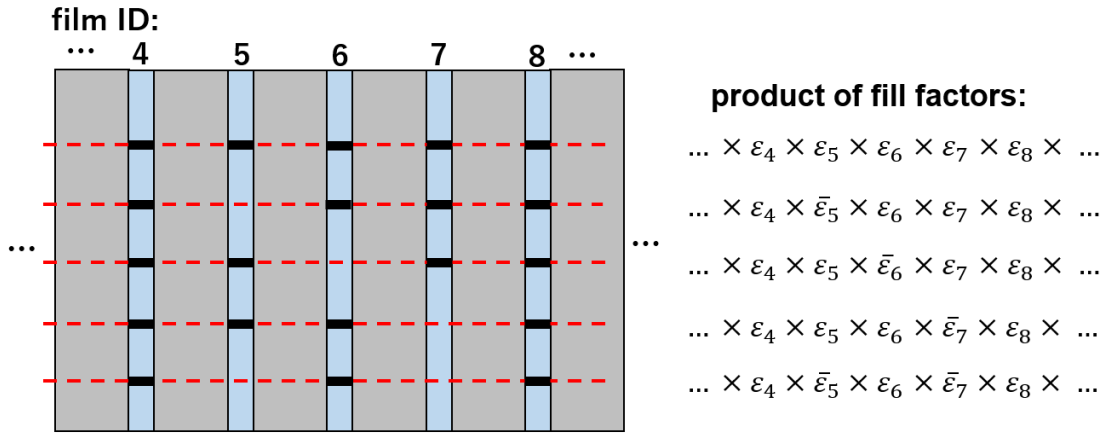

Figure 10. Example of all hit patterns and the products of fill factors in Eq. (4) when base tracks are found in film ID numbers 4 and 8. The red lines indicate the reconstructed tracks and the short black lines represent the base tracks found in the films.

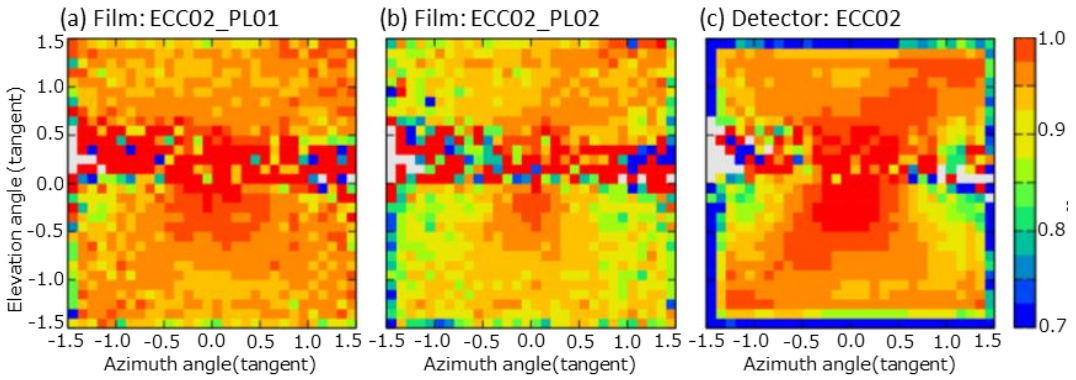

Figure 11. Examples of the angular distribution of the fill factor in some films and the efficiency of an ECC. (a) Fill factor for film ID = PL01 (most upstream film) and ECC ID = 02 at site "N". (b) Fill factor for film ID = PL02 and ECC ID = 02. (c) Muon detection efficiency for ECC ID = 02 as evaluated by Eq. (4). The horizontal axis is the tangent of azimuth angle; the vertical axis is the tangent of the elevation angle; the colors represent the fill factor/efficiency values. A positive elevation angle means the muon path is from the cone; a negative elevation angle means the muon path is from the backward free sky. The gray color means there were no observed muons in the angular bin due to the thick volcanic cone.

5 Results

The average density along muon path was determined for each observation site. We used the muon flux model of Honda et al. (2004), energy loss model of Groom et al. (2001), and topography around the Izu–Omuroyama scoria cone from the Geospatial Information Authority of Japan (https://maps.gsi.go.jp/). The coordinates of the observation site, direction, sensitive area, thickness of the ECC detectors, and observation time were used to calculate the expected number of muons at each observation site. The expected number of muons can be calculated as a function of the average density ρ_k along the path:

$$N_k^{simu}(\rho_k) = f_k(\rho_k, L_k) \times S_k \times \Omega_k \times T \times \epsilon_k \qquad (5)$$

where k is the index of an angular bin, $f_k(\rho_k, L_k)$ is the penetrating muon flux (calculated from the muon flux model, energy loss model, and path length L_k), S_k is the sensitive area of the ECC, Ω_k is the solid angle, ϵ_k is the muon detection efficiency, and T is the observation time.

The angular bin size used for calculating the expected value was $(0.01)^2$ in terms of the tangent. The angular bins were then merged to improve the statistical accuracy of the observed values. This merging procedure is useful in topology where a small change in elevation angle can dramatically change the path length in the volcano. If k is the index of the angular bins of $(0.01)^2$ and the bins belong to a larger angular bin i, then the following equation holds:

$$N_i^{merged}(\rho_i) = \sum_k N_k^{simu}(\rho_i) \quad (6)$$

where ρ_i is the density of the merged angular bin i. If N_i^{obs} is the number of the detected muons in the angular bin i, then we can uniquely determine the density value

ρ_i, such that $N_i^{merged}(\rho_i) = N_i^{obs}$. The lower limit ρ_i^{low} and upper limit ρ_i^{up} caused by the statistical error on N_i^{obs} can also be estimated as follows:

$$N_i^{merged}\left(\rho_i^{low}\right) = N_i^{obs} + \sqrt{N_i^{obs}} \quad (7)$$

$$N_i^{merged}\left(\rho_i^{up}\right) = N_i^{obs} - \sqrt{N_i^{obs}} \quad (8)$$

An example of the derived density map is shown in Fig. 12. All results are shown in Figs B1–B10 (Appendix B).

The definition of the angular bin areas was based on the following. The size of the angular bins was $(0.2)^2$ when the elevation angle is 0.1 to 0.5 in tangent terms. When the elevation angle is >0.5, the angular bin size was $(0.1)^2$. If the observed muon count in the bin was <25, the angular bin was manually merged with adjacent bins to improve the statistical error. The angular bin with a near-surface path (path length< 30 m) was excluded to avoid ambiguity between the actual topography and digital elevation map. The attitude errors of each muon detector also contribute to the path length ambiguity, especially near the surface of the cone.

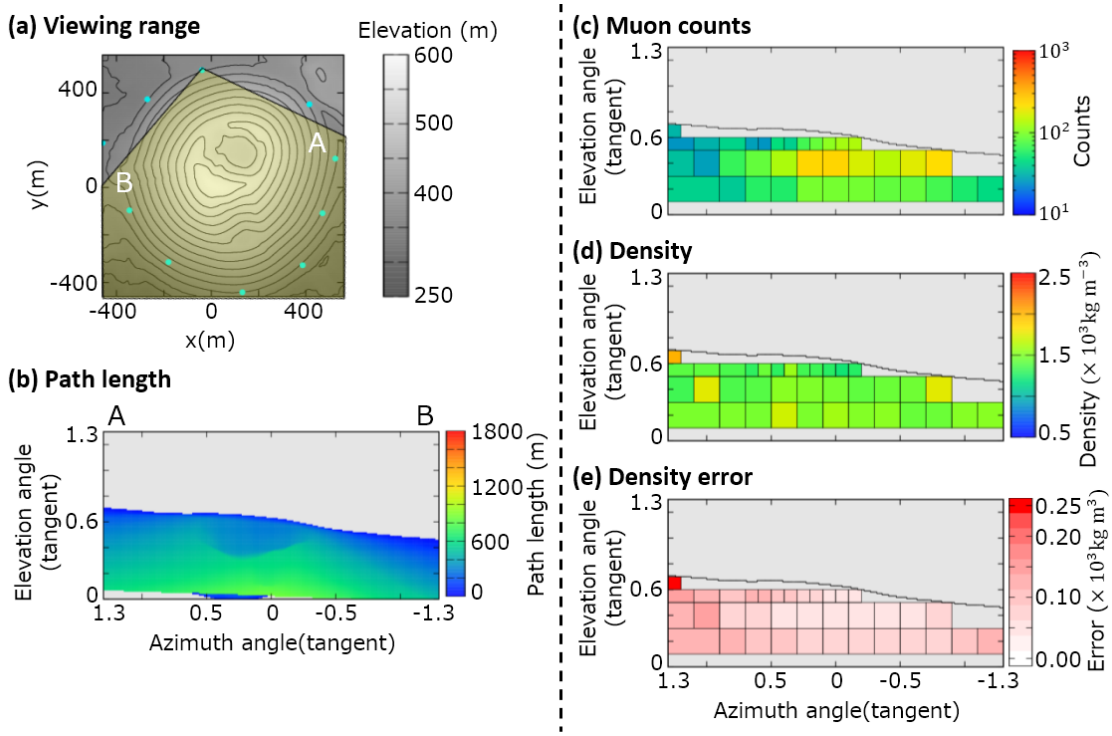

Figure 12. Data for observation site N. (a) Map, topography, and viewing range; (b) path length of the volcanic cone; (c) muon counts N_i^{obs}; (d) density ρ_i. The maximum value of the color bar indicates a density of >2.5 × 10^3 kg m^{-3} and the minimum value is <0.5 × 10^3 kg m^{-3}. (e) Density error $\Delta\rho = \left(\rho_i^{up} - \rho_i^{low}\right)/2$. The maximum value of the color bar indicates a density error of >0.25 × 10^3 kg m^{-3}.

6 Validation

Firstly, we validated the observed muon flux by comparing it with the muon flux model in the free sky region. The average and standard deviation of the ratio between the sites were 88% ± 4% in the forward direction and 92% ± 2% in the backward direction, except for the NNE site (Fig. 13). An example of observed/expected muon flux ratio angular distribution of the site N is shown in Fig. 14. As can be seen in this figure, in each detector site, the ununiform distribution of the observed/expected muon flux ratio exists. Such deviations were 4%–7% except the forward directions at the site SE and NNE. For reference, a 10% error on the flux corresponds to a 4% error on the density length at a tan(elevation angle) = 0.2 and density length = 1000 m (water equivalent). These deviations were less than the errors caused by the muon statistics. The discrepancy for the NNE site is discusses in the next section.

Secondly, we compared the density of the entire volcanic cone determined by gravity data with that obtained by muography. Table 2 shows the density determined from each observation site when the cone is assumed to be uniform. The calculation of the overall density $\bar{\rho}$ is as follows:

$$\bar{\rho} = \frac{\sum_i \rho_i V_i}{\sum_i V_i} \qquad (9)$$

where i is the index of the angular bins and V_i is the volume of the volcanic cone cut off by the angle bin i. Based on the gravity study of Nishiyama et al. (2021), the density of the Izu–Omuroyama scoria cone is $1.39 \pm 0.07 \times 10^3$ kg m^{-3}. The overall density derived by muography at each observation site is 1.42–1.53 $\times$ 10^3 kg m^{-3}, except for one site. These values are broadly consistent with the density determined from gravity data, except for the observation site W (1.72×10^3 kg m^{-3}).

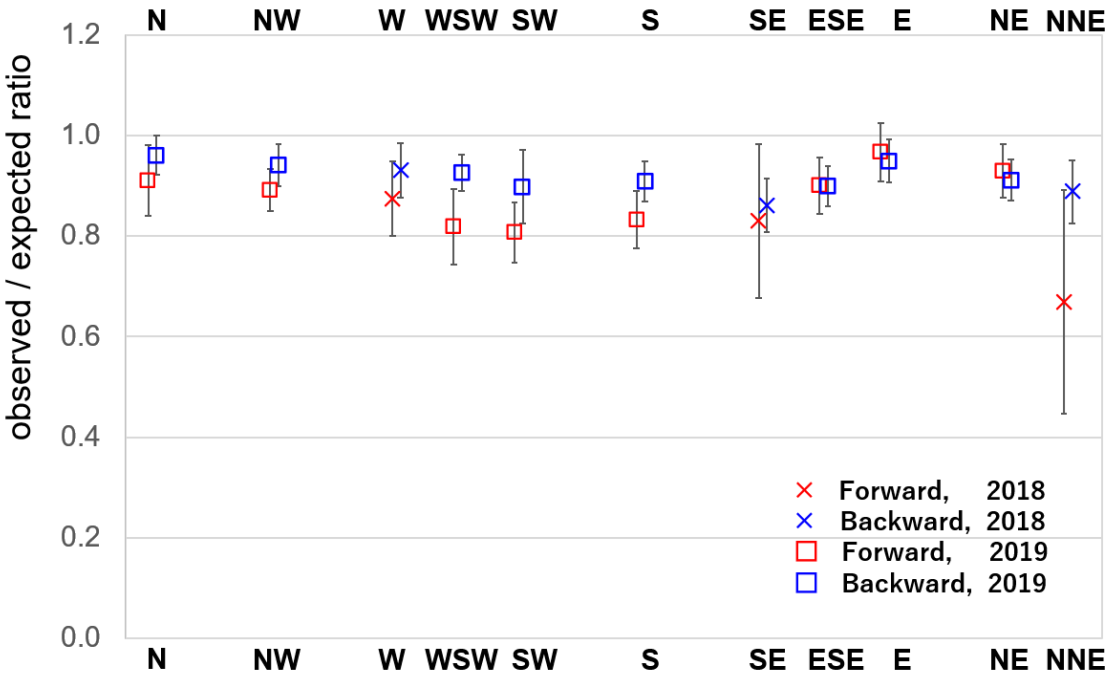

477

478 Figure 13. The observed/expected muon flux ratio for each observation site in the

479 free sky region. The plot represents the average value of the ratio in tangential

480 angular space, and the error bars are the standard deviations at each site.

481

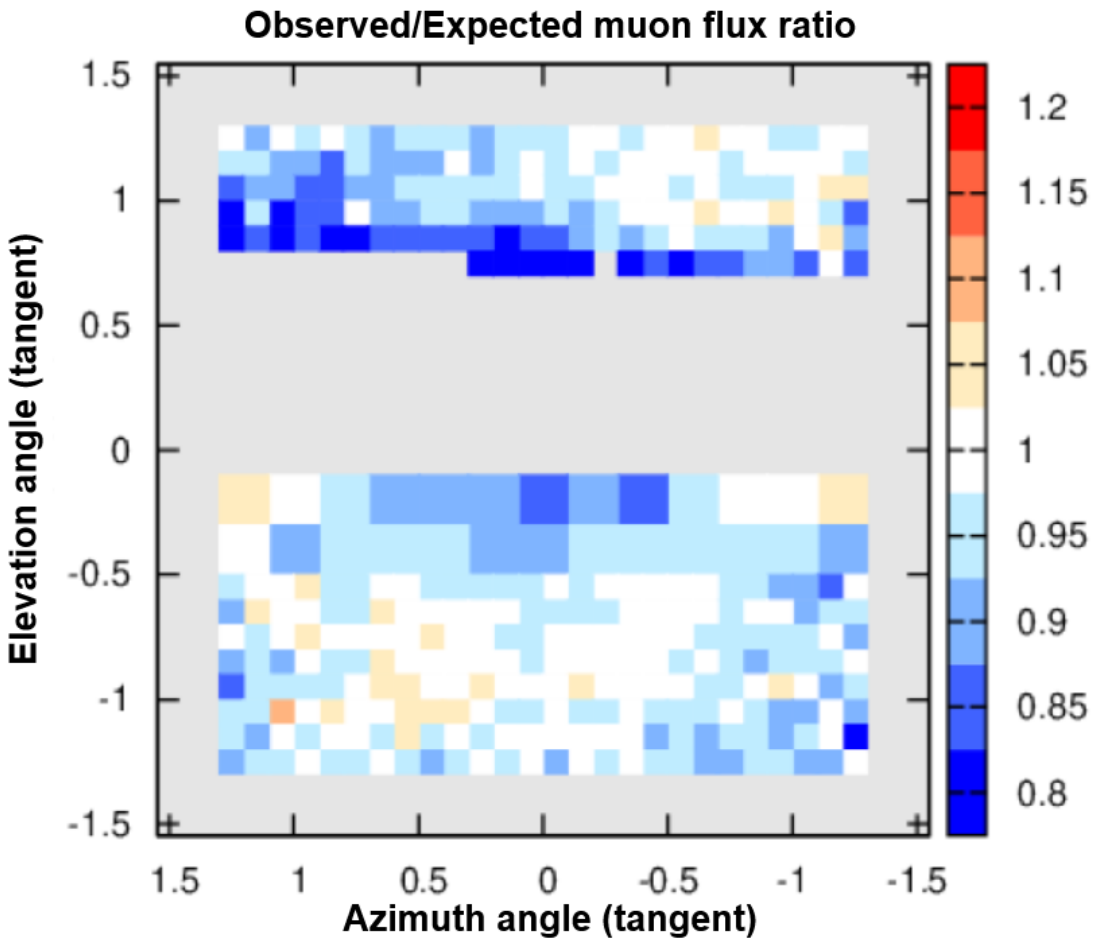

Figure 14. Example of the observed/expected muon flux ratio in the free sky region at site N. The horizontal axis represents azimuth angle, and the vertical axis represents the elevation angle. Positive elevation angle means the muons come from forward directions (the volcanic cone). Negative elevation angle means the muons come from backward free sky directions. Typical deviation of the ratio is 4%–7% in each site.

492

Observation site	Overall density $\bar{\rho}$ ($\times 10^3$ kg m^{-3})	Observation site	Overall density $\bar{\rho}$ ($\times 10^3$ kg m^{-3})
N	1.51	S	1.49
NW	1.45	ESE	1.45
W	1.72	E	1.42
WSW	1.50	NE	1.53
SE	1.46	NNE	1.50
SW	1.48		

493 Table 2. Overall bulk density obtained by muography, assuming that the density is

494 uniform in the volcanic cone.

495

7 Discussion

For the observed/expected muon flux ratio in the free sky region, the values in the forward direction are less than in the backward direction at many observation sites. This could be because the detectors were buried in holes on steep slopes (~30˚), and our analysis might not account for that effect. Due to the steep slope, muons arriving from the forward direction need to penetrate some amount of soil, whereas muons from the backward direction can enter the detector without being affected by the soil cover. In addition, the resolution of the detector coordinates is ~3 m, which might also contribute to the discrepancy.

Some density results from near the ground surface are complex. Some regions near the path length of 30 m appear to have relatively higher or lower density than the other data (e.g., Fig. B6, B9). One possible reason for this is the error on the detector attitude. Near the surface of the volcanic cone, the difference between the calculated and actual path lengths may become larger due to the error on the detector attitude.

The anomalous data for the NNE site also warrants further consideration. The reason for this might be a difference between the digital elevation map and actual topography. There is a stone wall in front of the buried detector at this site, which is about 1 m high and located on the volcanic cone side. The grid size of the digital elevation map used in this study is 1 m, and thus the map might not record this steep gradient.

In summary, errors in the position and attitude of the detectors, and the accuracy of the DEM, might cause a misfit between the DEM and actual topography. These are the main reasons for the discrepancy between the observed and expected muon flux.

The discrepancy between the observed and expected muon flux was ±4% in the forward direction and ±2% in the backward direction between the detectors. In

addition, the typical deviation inside each site was 4%–7%. These values are smaller than the statistical error of the observed muons used to determine the density of the volcanic cone, and thus they were not significant for our observations. It is interesting to consider if an improvement in the accuracy of the detector position and attitude, and the DEM, would decrease this systematic error. For example, the ±4% deviation in the forward direction would be expected to decrease to ±2%, because the misfit effect is less in the backward direction. Further improvements will require simulation of the expected muon flux that take into account more processes and verification of the systematic errors associated with the ECC detectors.

The obtained density values (1.42–1.53 × 10^3 kg m^{-3}; this study) and 1.39 ± 0.07 × 10^3 kg m^{-3} (Nishiyama et al., 2021) for Izu–Omuroyama scoria cone are broadly consistent (Table 2). In a previous study, Rosas-Carbajal et al. (2017) identified an offset between the density obtained by muon and gravity data and the density obtained from muon data was 0.5 × 10^3 kg m^{-3} less than that obtained from gravity data. In our validation, this discrepancy does not exist. As Rosas-Carbajal et al (2017) suggested, the discrepancy might be due to differences in the filtering performance for low-momentum particles shown in Fig. 9.

The higher density obtained at site W cannot be explained by the systematic errors described above. One possible reason for this is an actual high-density structure in front of the site. This hypothesis is consistent with the fact that lava flowed out from the crater lake to the west (Koyano et al., 1996).

8 Conclusions

A muographic study of the Izu–Omuroyama scoria cone was undertaken in 11 directions. The ECC detector design was optimized for quick installation in the field. We mounted the 11 detectors beneath the ground, surrounding the volcanic cone. The tracks of charged particles that passed through the ECCs were reconstructed using the automated emulsion track readout system HTS and NETSCAN 2.0 software. After track selection, including momentum filtering and efficiency estimation, the density profiles in 2D angular space were derived for each observation site. The methods described in this paper can be applied to the observation of other volcanoes and target objects.

We compared the observed muon flux to the expected value from a muon flux model in the free sky region. The muon flux difference between each detector was 4% in the forward directions and 2% in the backward directions, and the typical deviations in each site were about 4%–7%. The errors on the detector coordinates and attitude, and DEM, are the main cause of the discrepancy between the observed and expected muon flux.

In addition, we also compared our results with the overall volcanic cone density estimated from gravity data, which are broadly consistent, apart from the W site. This discrepancy for the W site can be explained by the systematic errors discussed in the previous section and statistical error of the observed muons. It might also reflect a high-density structure located in the western flank of the volcano. Further 3D density reconstructions of the Izu–Omuroyama scoria cone are ongoing using the data set described in this paper.

Acknowledgements

The authors thank Hideaki Aoki and his colleagues of Ike-kankou for collaborating on our study. We also thank Masakazu Ichikawa of the Earthquake Research Institute, the University of Tokyo, for support during the observation campaign. We are also grateful for the technical support of the staff and students in F-lab, Nagoya University, especially with the nuclear emulsion films. This research was supported by JSPS KAKENHI Grant 19H01988, an Izu Peninsula Geopark Academic Research Grant (2018), the Joint Research Program of the Institute of Materials and Systems for Sustainability at Nagoya University (2017–2021), and a JSPS Fellowship (Nagahara; Grant DC2, 19J13805).

577 **References**

578 Agafonova, N., Aleksandrov, A., Altinok, O., Anokhina, A., Aoki, S., Ariga, A., Ariga, T.,
579 Autiero, D., Badertscher, A., Bagulya, A., Ben Dhahbi, A., Bertolin, A., Besnier, M.,
580 Bozza, C., Brugière, T., Brugnera, R., Brunet, F., Brunetti, G., Buontempo, S., Cazes,
581 A., Chaussard, L., Chernyavskiy, M., Chiarella, V., Chukanov, A., D'Ambrosio, N., Dal
582 Corso, F., De Lellis, G., del Amo Sanchez, P., Déclais, Y., De Serio, M., Di Capua, F., Di
583 Crescenzo, A., Di Ferdinando, D., Di Marco, N., Dmitrievski, S., Dracos, M.,
584 Duchesneau, D., Dusini, S., Dzhatdoev, T., Ebert, J., Egorov, O., Enikeev, R., Ereditato,
585 A., Esposito, L. S., Favier, J., Ferber, T., Fini, R. A., Frekers, D., Fukuda, T.,
586 Garfagnini, A., Giacomelli, G., Giorgini, M., Göllnitz, C., Goldberg, J., Golubkov, D.,
587 Goncharova, L., Gornushkin, Y., Grella, G., Grianti, F., Guler, A. M., Gustavino, C.,
588 Hagner, C., Hamada, K., Hara, T., Hierholzer, M., Hollnagel, A., Hoshino, K., Ieva, M.,
589 Ishida, H., Jakovcic, K., Jollet, C., Juget, F., Kamiscioglu, M., Kazuyama, K., Kim, S.
590 H., Kimura, M., Kitagawa, N, Klicek, B., Knuesel, J., Kodama, K., Komatsu, M., Kose,
591 U., Kreslo, I., Kubota, H., Lazzaro, C., Lenkeit, J., Lippi, I., Ljubicic, A., Longhin, A.,
592 Loverre, P., Lutter, G., Malgin, A., Mandrioli, G., Manai, K., Marteau, J., Matsuo, T.,
593 Matveev, V., Mauri, N., Medinaceli, E., Meisel, F., Meregaglia, A., Migliozzi, P.,
594 Mikado, S., Miyamoto, S., Monacelli, P., Morishima, K., Moser, U., Muciaccia, M. T.,
595 Naganawa, N., Naka, T., Nakamura, M., Nakano, T., Naumov, D., Nikitina, V., Niwa,
596 K., Nonoyama, Y., Ogawa, S., Okateva, N., Olshevskiy, A., Paniccia, M., Paoloni, A.,
597 Park, B. D., Park, I. G., Pastore, A., Patrizii, L., Pennacchio, E., Pessard, H., Pretzl, K.,
598 Pilipenko, V., Pistillo, C., Polukhina, N., Pozzato, M., Pupilli, F., Rescigno, R.,
599 Roganova, T., Rokujo, H., Romano, G., Rosa, G., Rostovtseva, I., Rubbia, A., Russo, A.,
600 Ryasny, V., Ryazhskaya, O., Sato, O., Sato, Y., Schembri, A., Schmidt-Parzefall, W.,

Schroeder, H., Scotto Lavina, L., Sheshukov, A., Shibuya, H., Shoziyoev, G., Simone, S., Sioli, M., Sirignano, C., Sirri, G., Song, J. S., Spinetti, M., Stanco, L., Starkov, N., Stipcevic, M., Strauss, T., Strolin, P., Takahashi, S., Tenti, M., Terranova, F., Tezuka, I., Tioukov, V., Tolun, P., Trabelsi, A., Tran, T., Tufanli, S., Vilain, P., Vladimirov, M., Votano, L., Vuilleumier, J. L., Wilquet, G., Wonsak, B., Yakushev, V., Yoon, C. S., Yoshioka, T., Yoshida, J., Zaitsev, Y., Zemskova, S., Zghiche, A., and Zimmermann, R.: Momentum measurement by the multiple Coulomb scattering method in the OPERA lead-emulsion target, New J. Phys., 14, 013026, https://doi.org/10.1088/1367-2630/14/1/013026, 2012.

Aramaki, S., and Hamuro, K.: Geology of the Higasi–Izu monogenetic volcano group, Bull. Earthq. Res. Inst. Univ. Tokyo, 52, 235–278, https://repository.dl.itc.u-tokyo.ac.jp/record/33207/files/ji0522010.pdf, 1977. (in Japanese)

Bozza, C., D'Ambrosio, N., De Lellis, G., De Serio, M., Di Capua, F., Di Crescenzo, A., Di Ferdinando, D., Di Marco, N., Esposito, L. S., Rosa Anna Fini, R. A., Giacomelli, G., Grella, G., Ieva, M., Kose, U., Longhin, A., Mauri, N., Medinaceli, E., Monacelli, P., Muciaccia, M. T., Pastore, A., Patrizii, L., Pozzato, M., Pupilli, F., Rescigno, R., Romano, G., Rosa, G., Ruggieri, A., Russo, A., Simone, S., Sirignano, C., Sirri, G., Stellacci, S. M., Tenti, M., Tioukov, V., Togo, V., and Valieri, C.: An integrated system for large scale scanning of nuclear emulsions, Nucl. Instrum. Methods Phys. Res. A, 703, 1, 204–212, https://doi.org/10.1016/j.nima.2012.11.099, 2012.

Bush, A. L.: Construction Materials: Lightweight Aggregates, in "Encyclopedia of

625 Materials: Science and Technology", Elsevier, pp 1550–1558, https://doi.org/10.1016/B0-
626 08-043152-6/00277-1, 2001.
627
628 Geshi, N., and Neri, M.: Dynamic feeder dyke systems in basaltic volcanoes: the
629 exceptional example of the 1809 Etna eruption (Italy), Front. Earth Sci., 2, 13,
630 https://doi.org/10.3389/feart.2014.00013, 2014.
631
632 Groom, D. E., Mokhov, N. V., and Striganov, S. I.: Muon stopping power and range
633 tables 10 MeV–100 TeV, At. Data Nucl. Data Tables , 78, 183–356,
634 https://doi.org/10.1006/adnd.2001.0861, 2001.
635
636 Hamada, K., Fukuda, T., Ishiguro, K., Kitagawa, N., Kodama, K., Komatsu, M.,
637 Morishima, K., Nakano, T., Nakatsuka, Y., Nonoyama, Y., Sato, O., and Yoshida, J.:
638 Comprehensive track reconstruction tool "NETSCAN 2.0" for the analysis of the
639 OPERA Emulsion Cloud Chamber, J. Instrum., 7, P07001, https://doi.org/10.1088/1748-
640 0221/7/07/P07001, 2012.
641
642 Hamuro, K.: Petrology of the Higashi–Izu monogenetic volcano group, Bull. Earthq.
643 Res. Inst. Univ. Tokyo, 60, 335–400, https://repository.dl.itc.u-
644 tokyo.ac.jp/record/32886/files/ji0603001.pdf, 1985.
645
646 Hiramoto, A., Suzuki, Y., Ali, A., Aoki, S., Berns, L., Fukuda, T., Hanaoka, Y., Hayato,
647 Y., Ichikawa, A. K., Kawahara, H., Kikawa, T., Koga, T., Komatani, R., Komatsu, M.,
648 Kosakai, Y., Matsuo, T., Mikado, S., Minamino, A., Mizuno, K., Morimoto, Y.,

649 Morishima, K., Naganawa, N., Naiki, M., Nakamura, M., Nakamura, Y., Nakano, N.,
650 Nakano, T., Nakaya, T., Nishio, A., Odagawa, T., Ogawa, S., Oshima, H., Rokujo, H.,
651 Sanjana, I., Sato, O., Shibuya, H., Sugimura, K., Suzui, L., Takagi, H., Takao, T.,
652 Tanihara, Y., Yasutome, K., and Yokoyama, M. (NINJA Collaboration): First
653 measurement of $\underline{\nu}_\mu$ and ν_μ charged-current inclusive interactions on water using a
654 nuclear emulsion detector, Phys. Rev. D, 102, 072006,
655 https://doi.org/10.1103/PhysRevD.102.072006, 2020.
656
657 Honda, M., Kajita, T., Kasahara, K., and Midorikawa, S.: New calculation of the
658 atmospheric neutrino flux in a three-dimensional scheme, Phys. Rev. D, 70, 043008,
659 https://doi.org/10.1103/PhysRevD.70.043008, 2004.
660
661 Jourde, K., Gibert, D., and Marteau, J.: Improvement of density models of geological
662 structures by fusion of gravity data and cosmic muon radiographies, Geosci. Instrum.
663 Methods Data Syst., 4, 177–188, https://doi.org/10.5194/gi-4-177-2015, 2015.
664
665 Jourde, K., Gibert, D., Marteau, J., d'Ars, J.B., and Komorowski, J.C.: Muon dynamic
666 radiography of density changes induced by hydrothermal activity at the La Soufrière of
667 Guadeloupe volcano, Sci. Rep., 6, 33406, https://doi.org/10.1038/srep33406, 2016.
668
669 Kereszturi, G., and Németh, K.: Monogenetic Basaltic Volcanoes: Genetic
670 Classification, Growth, Geomorphology and Degradation, Updates in Volcanology—
671 New Advances in Understanding Volcanic Systems, Karoly Nemeth, IntechOpen., DOI:
672 10.5772/51387, 2012.

673

674 Kodama, K., Hoshino, K., Komatsu, M., Miyanishi, M., Nakamura, M., Nakamura, T.,
675 Nakano, T., Narita, K., Niwa, K., Nonaka, N., Sato, O., Toshito, T., and Uetake, T.:
676 Study of electron identification in a few GeV region by an emulsion cloud chamber,
677 Rev. Sci. Instrum., 74, 53, https://doi.org/10.1063/1.1529300, 2003.

678

679 Koyama, M.: Photographs of the Izu-peninsula by UAV, Iwanami Science Library 268,
680 Iwanami Shoten, Publishers, Tokyo, 159 pp, ISBN 9784000296687, 2017. (in Japanese)

681

682 Koyano, Y., Hayakawa, Y., and Machida, H.: The eruption of Omuroyama in the
683 Higashi Izu monogenetic volcano field, J Geog. (Chigaku Zasshi), 105, 4, 475–484,
684 https://doi.org/10.5026/jgeography.105.4_475, 1996. (in Japanese)

685

686 Kreslo, I., Cozzi, M., Ereditato, A., Hess, M., Knuesel, J., Laktineh, I., Messina, M.,
687 Moser, U., Pistillo, C., and Pretzl, K.: High-speed analysis of nuclear emulsion films
688 with the use of dry objective lenses, J. Instrum., 3, P04006,
689 https://dx.doi.org/10.1088/1748-0221/3/04/P04006, 2008.

690

691 Morishima, K., and Nakano, T.: Development of a new automatic nuclear emulsion
692 scanning system, S-UTS, with continuous 3D tomographic image read-out, J. Instrum.,
693 5, P04011, http://dx.doi.org/10.1088/1748-0221/5/04/P04011, 2010.

694

695 Morishima, K., Kuno, M., Nishio, A., Kitagawa, N., Manabe, Y., Moto, M., Takasaki, F.,
696 Fujii, H., Satoh, K., Kodama, H., Hayashi, K., Odaka, S., Procureur, S., Attie, D.,

Bouteille, S., Calvet, D., Filosa, C., Magnier, P., Mandjavidze, I., Riallot, M., Marini, B., Gable, P., Date, Y., Sugiura, M., Elshayeb, Y., Elnady, T., Ezzy, M., Guerriero, E., Steiger, V., Serikoff, N., Mouret, J., Charles, B., Helal, H., and Tayoubi, M.: Discovery of a big void in Khufu's Pyramid by observation of cosmic-ray muons, Nature, 552, 387, https://doi.org/10.1038/nature24647, 2017.

Nagahara, S., and Miyamoto, S.: Feasibility of three-dimensional density tomography using dozens of muon radiographies and filtered back projection for volcanoes, Geosci. Instrum. Methods Data Syst., 7, 307–316, https://doi.org/10.5194/gi-7-307-2018, 2018.

Nakamura, T., Ariga, A., Ban, T., Fukuda, T., Fukuda, T., Fujioka, T., Furukawa, T., Hamada, K., Hayashi, H., Hiramatsu, S., Hoshino, K., Kawada, J., Koike, N., Komatsu, M., Matsuoka, H., Miyamoto, S., Miyanishi, K., Miyanishi, M., Morishima, K., Nada, H., Naganawa, N., Nakano, T., Narita, K., Natsume, M., Niwa, K., Nonaka, N., Park, B. D., Sato, O., Takahashi, S., Toshito, T., Uetake, T., Nakamura, M., Kuwabara, K., Nishiyama, S., Nonoyama, Y., and Kodama, K.: The OPERA film: New nuclear emulsion for large-scale, high-precision experiments, Nucl. Instrum. Methods Phys. Res. A, 556, 1, 80–86, https://doi.org/10.1016/j.nima.2005.08.109, 2005.

Nishio, A., Morishima, K., Kuwabara, K., Yoshida, T., Funakubo, T., Kitagawa, N., Kuno, M., Manabe, Y., and Nakamura, M.: Nuclear emulsion with excellent long-term stability developed for cosmic-ray imaging, Nuclear Instruments and Methods in Physics Research A, 966, 163850, https://doi.org/10.1016/j.nima.2020.163850, 2020.

721 Nishiyama, R., Miyamoto, S., and Naganawa, N.: Experimental study of source of
722 background noise in muon radiography using emulsion film detectors, Geosci. Instrum.
723 Methods Data Syst., 3, 29–39, https://doi.org/10.5194/gi-3-29-2014, 2014.
724
725 Nishiyama, R., Miyamoto, S., Okubo, S., Oshima, H., and Maekawa, T.: 3D density
726 modeling with gravity and muon-radiographic observations in Showa–Shinzan lava
727 dome, Usu, Japan, Pure Appl. Geophys., 174, 1061–1070,
728 https://doi.org/10.1007/s00024-016-1430-9, 2017.
729
730 Nishiyama, R., Miyamoto, S., and Nagahara, S.: Estimation of the bulk density of the
731 Omuro scoria cone (eastern Izu, Japan) from gravity survey, Bull. Earthq. Res. Inst.
732 Univ. Tokyo, 95, 1–7, https://repository.dl.itc.u-
733 tokyo.ac.jp/record/2000093/files/IHO951401.pdf, 2020.
734
735 Oláh, L., Tanaka, H. K. M., Ohminato, T., and Varga, D.: High-definition and low-noise
736 muography of the Sakurajima volcano with gaseous tracking detectors, Sci. Rep., 8,
737 3207, https://doi.org/10.1038/s41598-018-21423-9, 2018.
738
739 Rosas-Carbajal, M., Jourde, K., Marteau, J., Deroussi, S., Komorowski, J.-C., and
740 Gibert, D.: Three-dimensional density structure of La Soufrière de Guadeloupe lava
741 dome from simultaneous muon radiographies and gravity data, Geophys. Res. Lett., 44,
742 6743–6751, https://doi.org/10.1002/2017GL074285, 2017.
743
744 Saito, T., Takahashi, S., and Wada, H.: ^{14}C ages of Omuroyama Volcano, Izu Peninsula,

745 Bull. Volcanol. Soc. Jpn. , 48, 215–219, https://doi.org/10.18940/kazan.48.2_215, 2003.
746 (in Japanese)
747
748 Saracino, G., Amato, L., Ambrosino, F., Antonucci, G., Bonechi, L., Cimmino, L.,
749 Consiglio, L., D'Alessandro, R., De Luzio, E., Minin, G., Noli, P., Scognamiglio, L.,
750 Strolin, P., and Varriale, A.: Imaging of underground cavities with cosmic-ray muons
751 from observations at Mt. Echia (Naples), Sci. Rep., 7, 1181,
752 https://doi.org/10.1038/s41598-017-01277-3, 2017.
753
754 Taha, A. A., and Mohamed, A. A.: Chemical, physical and geotechnical properties
755 comparison between scoria and pumice deposits in Dhamar–Rada Volcanic Field, SW
756 Yemen, Aust. J. Basic & Appl. Sci., 7, 11, 116–124,
757 http://www.ajbasweb.com/old/ajbas/2013/September/116-124.pdf, 2013.
758
759 Takahashi, S., Aoki, S., Kamada, K., Mizutani, S., Nakagawa, R., Ozaki, K., and
760 Rokujo, H.: GRAINE project: The first balloon-borne, emulsion gamma-ray telescope
761 experiment, Prog. Theor. Exp. Phys., 4, https://doi.org/10.1093/ptep/ptv046, 2015.
762
763 Tanahashi, M., et al. (Particle Data Group), Phys. Rev. D 98, 030001,
764 https://doi.org/10.1103/PhysRevD.98.030001, 2018.
765
766 Tanaka, H. K. M., Nakano, T., Takahashi, S., Yoshida, J., Takeo, M., Oikawa, J.,
767 Ohminato, T., Aoki, Y., Koyama, E., Tsuji, H., and Niwa, K.: High resolution imaging
768 in the inhomogeneous crust with cosmic-ray muon radiography: The density structure

769 below the volcanic crater floor of Mt. Asama, Japan, Earth Planet. Sci. Lett., 263, 1–2,
770 104–113, https://doi.org/10.1016/j.epsl.2007.09.001, 2007.
771
772 Tanaka, H. K. M., Uchida, T., Tanaka, M., Shinohara, H., and Hideaki, T.: Cosmic-ray
773 muon imaging of magma in a conduit: Degassing process of Satsuma–Iwojima Volcano,
774 Japan, Geophys. Res. Lett., 36, L01304, https://doi.org/10.1029/2008GL036451, 2009.
775
776 Tanaka, H. K. M., Taira, H., Uchida, T., Tanaka, M., Takeo, M., Ohminato, T., and
777 Tsuji, H.: Three-dimensional computational axial tomography scan of a volcano with
778 cosmic ray muon radiography, J. Geophys. Res. Solid Earth, 115, B12332,
779 https://doi.org/10.1029/2010JB007677, 2010.
780
781 Tanaka, H. K. M., Kusagaya, T., and Shinohara, H.: Radiographic visualization of
782 magma dynamics in an erupting volcano, Nat. Commun., 5, 3381,
783 https://doi.org/10.1038/ncomms4381, 2014.
784
785 Tioukov, V., Alexandrov, A., Bozza, C., Consiglio, L., D'Ambrosio, N., De Lellis, G., De
786 Sio, C., Giudicepietro, F., Macedonio, G., Miyamoto, S., Nishiyama, R., Orazi, M.,
787 Peluso, R., Sheshukov, A., Sirignano, C., Stellacci, S. M., Strolin, P., and Tanaka, H. K.
788 M.: First muography of Stromboli volcano, Sci. Rep., 9, 6695,
789 https://doi.org/10.1038/s41598-019-43131-8, 2019.
790
791 Watanabe, A., Takenaka, H., Fujii, Y., and Fujiwara, H.: Seismometer azimuth
792 measurement at K-NET station (2): Oita Prefecture, Zisin, 53, 185–192,

https://doi.org/10.4294/zisin1948.53.2_185, 2000. (in Japanese)

Yamamoto, H.: The mode of lava outflow from cinder cones in the Ojika–Jima monogenetic volcano group, Bull. Volcanol. Soc. Jpn., 48, 1, https://doi.org/10.18940/kazan.48.1_11, 2003. (in Japanese)

Yoshimoto, M., Nakano, T., Komatani, R., and Kawahara, H.: Hyper-track selector nuclear emulsion readout system aimed at scanning an area of one thousand square meters, Prog. Theor. Exp. Phys., 2017, 10, https://doi.org/10.1093/ptep/ptx131, 2017.

Appendix A

We here consider how the position dependency of the detected tracks affects the density results.

The fill factor of the base tracks (i.e., track detection efficiency in a film) also depends on the position of the scanned film. The typical causes of the decrease of the fill factor are heterogeneous thickness of the emulsion layers, some dusts or scratches on the emulsion surface, and the poorly tuned parameters for the scanning.

Fig. A1 shows the position distribution of the fill factor of all films of an ECC. For example, at upper right the films tend to have the low fill factor (e.g., a-f, h, k, l, q). This part has the larger thickness of emulsion layer because the drops of glycerin solution were left in the upper right corner when drying after soaking due to the structure of developing racks. Fig. A1(s) and (t) have larger area of low fill factor in the right and left. The reason might be the poorly tuned parameters for the scanning.

Compared to the size of the scoria cone, the ECC is a very small "element", thus the local position dependence of the fill factor can be approximately treated as an average fill factor $\varepsilon_j(\theta_x, \theta_y)$. The decrease of the fill factor is reflected in the $\varepsilon_j(\theta_x, \theta_y)$ in Eq. (4). Finally, $\varepsilon_j(\theta_x, \theta_y)$, which encompasses the effects of the local decrease of the fill factor, is effectively used to derive the angle-dependent muon detection efficiency.

We should also consider the position dependency of noise. Local high density of random silver grains caused by any chemical conditions, or fake images produced by scratches on the films tend to create a group of fake tracks concentrated in one place. In addition, such fake tracks tend to have small slopes by scanning with automated emulsion readout system. If such noise is continuous at the same location on the film, they might make many parallel tracks at a certain slope and give a systematic error in the result. However, such possibility has been eliminated by the track selection algorithm described in the section 4.2. Because such concentrated tracks in position and angular space make numerous branches in track connection (see Fig. 6) and tracks with such branches were removed in the selection procedure. Fig. A2 shows the number of selected tracks with small slope per mm^2 in each observation site. The histogram roughly fits the Poisson distribution and there is no remarkable excess. The difference of the peak in the histograms depends on the difference of exposure time (SE, W, NNE), existence of topography in the backward direction (NE), pitch angle of the detector attitude (e.g., SW has larger pitch angle, thus less tracks of the small slopes from the backward direction), and the difference of muon detection efficiency.

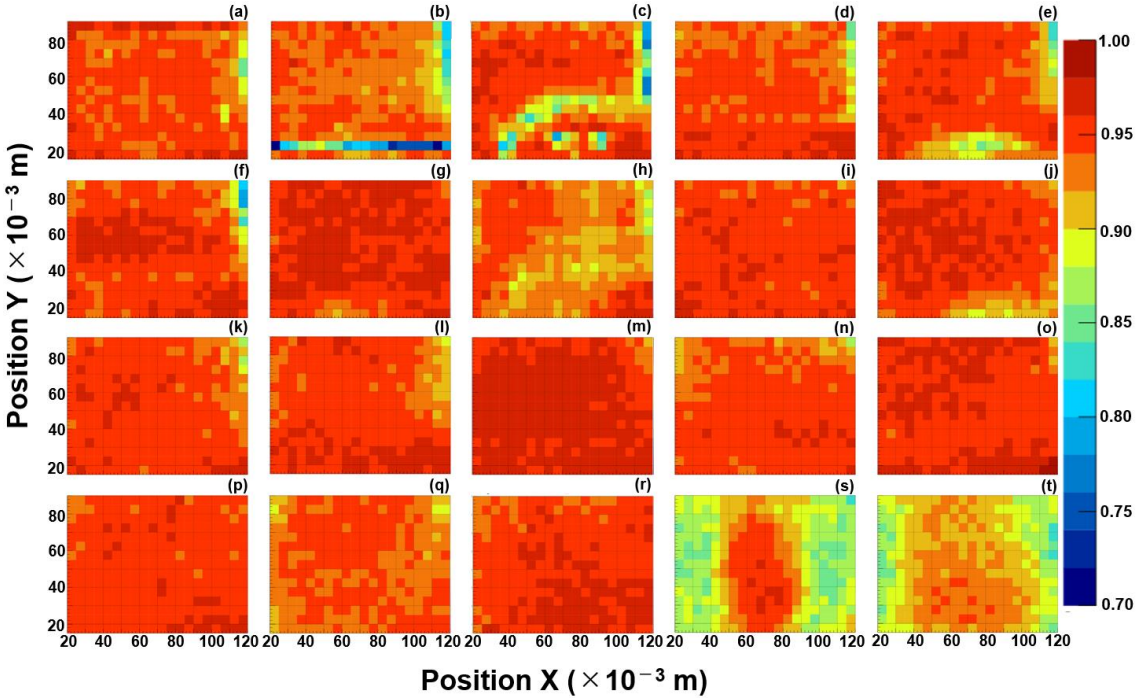

Figure A1. The position distribution of the fill factor in each film of ECC02. (a)–(t) represent PL01–PL20, respectively.

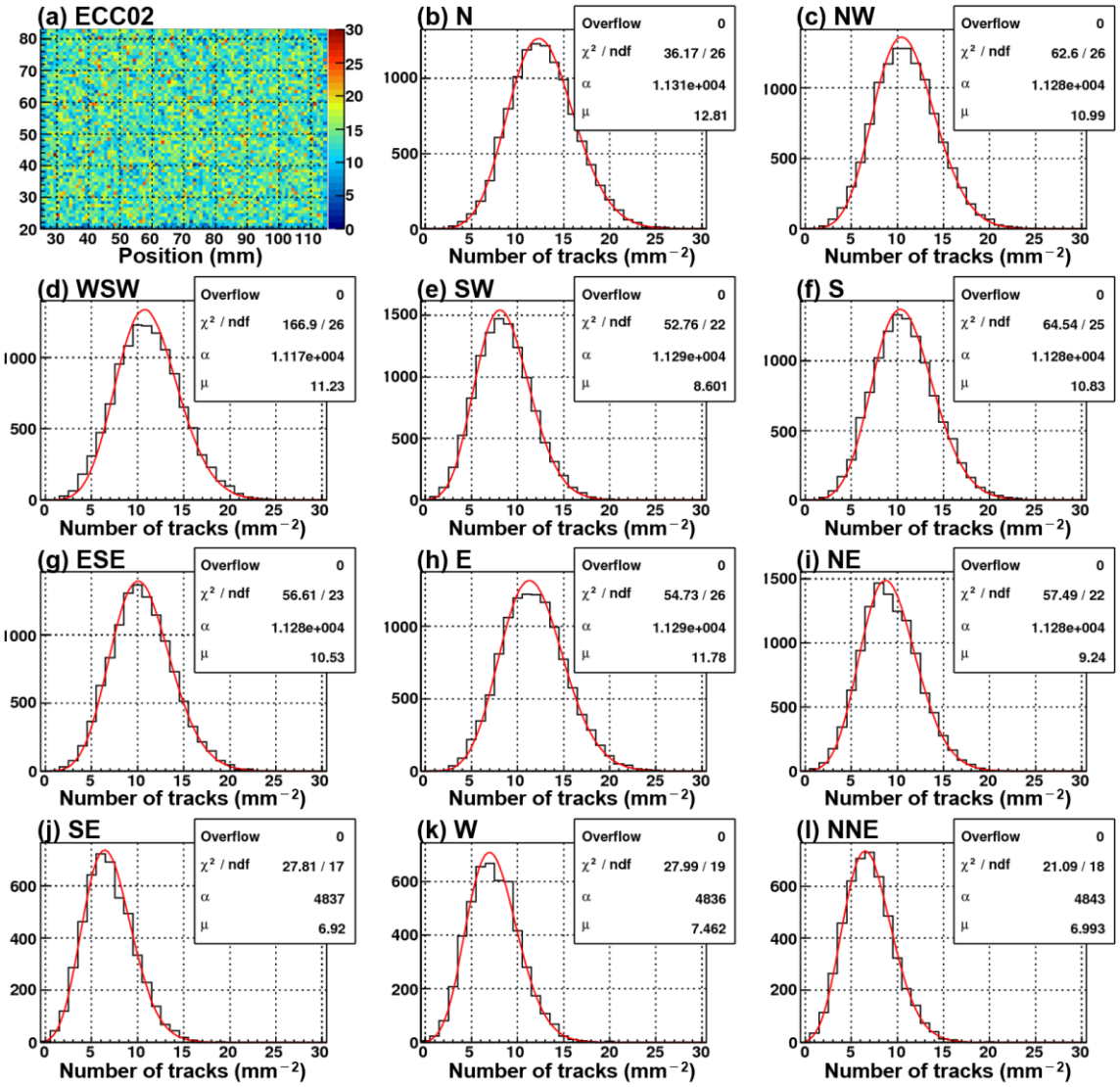

Figure A2. (a) The position distribution of the number of the selected tracks per mm² in the ECC02. (b)–(l) The number of the selected tracks per mm² (the black line) with the fitting result of Poisson distribution ($= \alpha\mu^{x}e^{-\mu}/x!$, the red line) in each observation site, respectively. The tracks selected for this figure came from in the backward direction and have small slopes ($|\tan\theta_x| < 0.5$ and $|\tan\theta_y| < 0.5$).

Appendix B

The density results for each observation site are shown in Figs B1–B10.

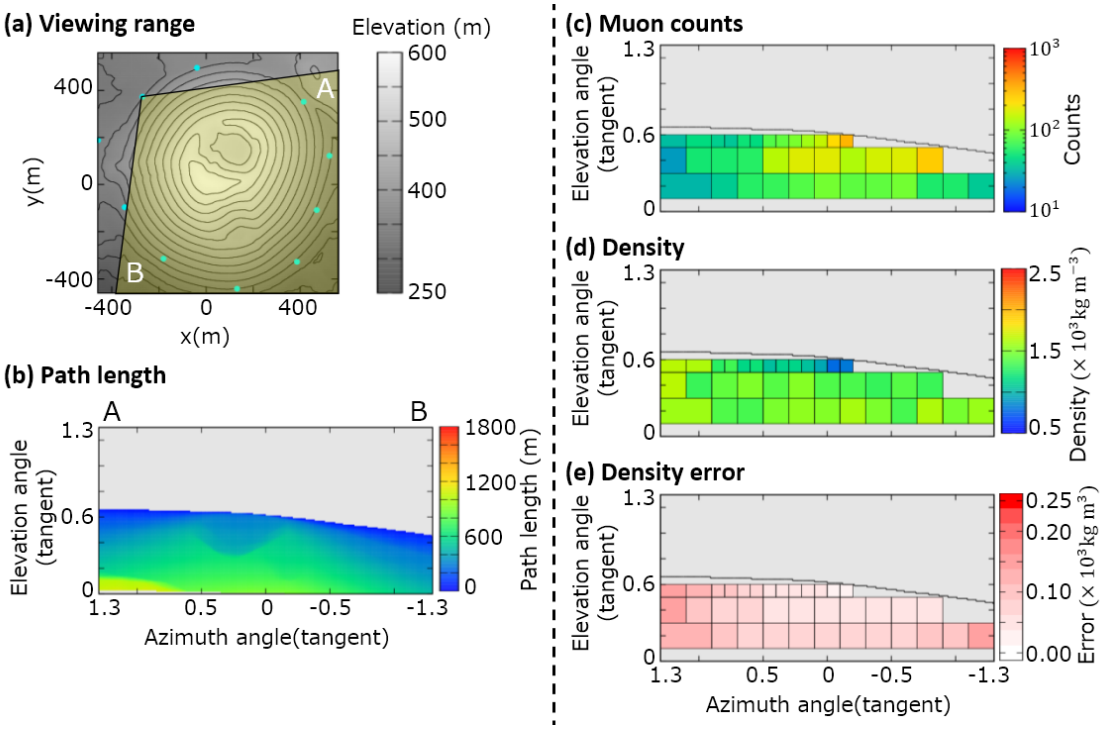

Figure B1. Observation site NW. (a) Map, topography, and viewing range; (b) path length of the volcanic cone; (c) muon counts N_i^{obs}; (d) density ρ_i. The maximum value of the color bar indicates a density of >2.5 × 10^3 kg m^{-3} and the minimum value is <0.5 × 10^3 kg m^{-3}. (e) Density error $\Delta\rho = (\rho_i^{up} - \rho_i^{low})/2$. The maximum value of the color bar indicates a density error of >0.25 × 10^3 kg m^{-3}.

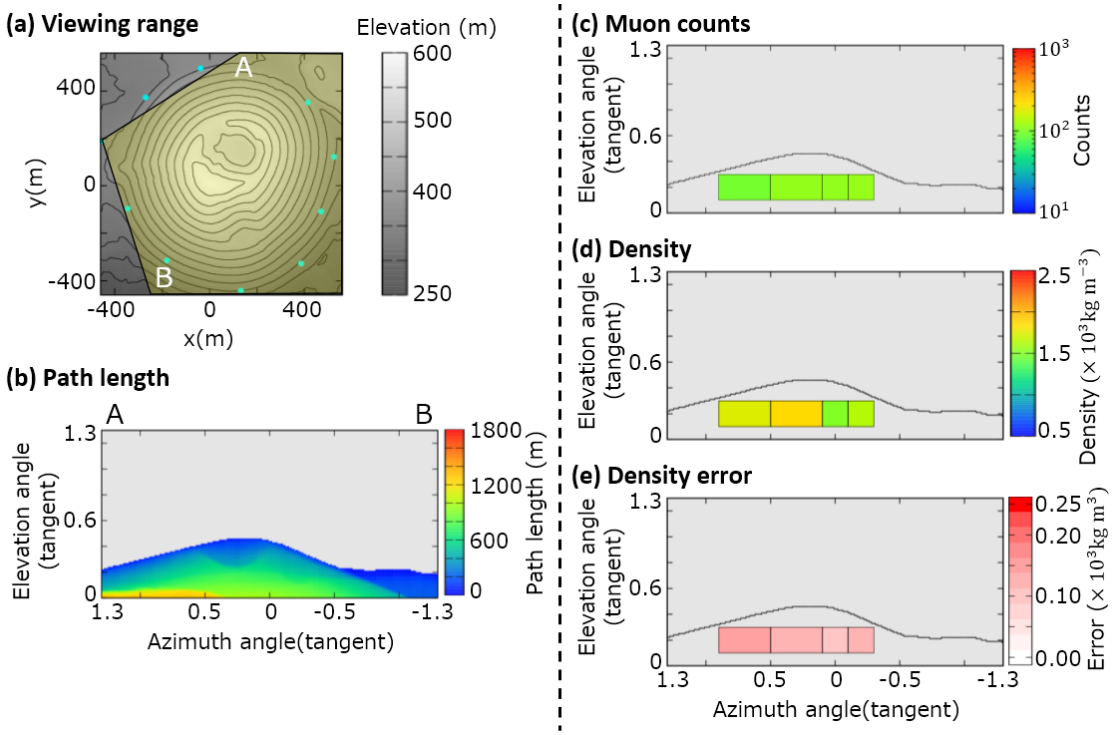

Figure B2. Observation site W. (a) Map, topography, and viewing range; (b) path length of the volcanic cone; (c) muon counts N_i^{obs}; (d) density ρ_i. The maximum value of the color bar indicates a density of >2.5 × 10^3 kg m^{-3} and the minimum value is <0.5 × 10^3 kg m^{-3}. (e) Density error $\Delta\rho = \left(\rho_i^{up} - \rho_i^{low}\right)/2$. The maximum value of the color bar indicates a density error of >0.25 × 10^3 kg m^{-3}.

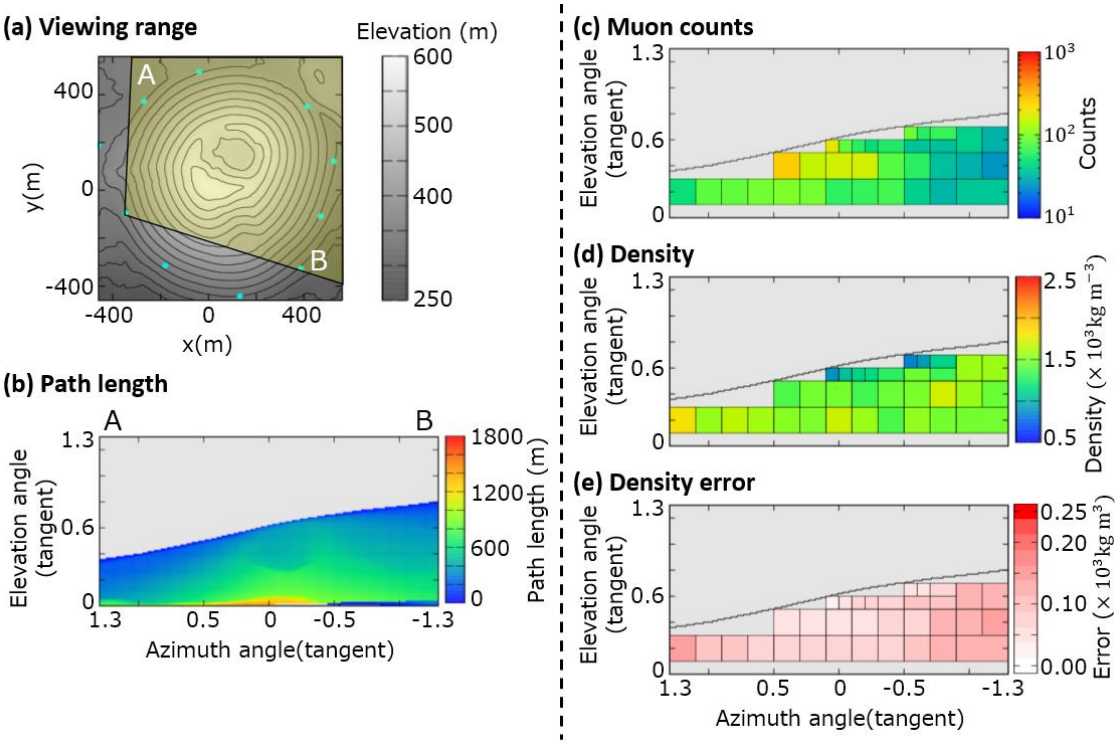

Figure B3. Observation site WSW. (a) Map, topography, and viewing range; (b) path length of the volcanic cone; (c) muon counts N_i^{obs}; (d) density ρ_i. The maximum value of the color bar indicates a density of >2.5 × 10^3 kg m^{-3} and the minimum value is <0.5 × 10^3 kg m^{-3}. (e) Density error $\Delta\rho = \left(\rho_i^{up} - \rho_i^{low}\right)/2$. The maximum value of the color bar indicates a density error of >0.25 × 10^3 kg m^{-3}.

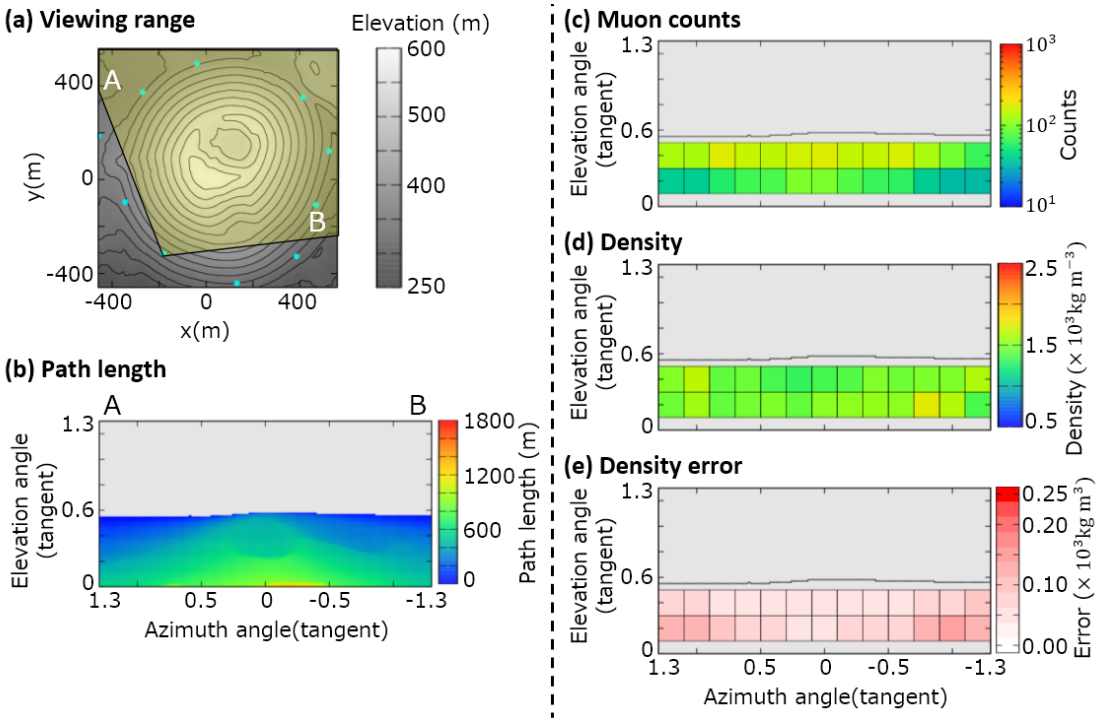

Figure B4. Observation site SW. (a) Map, topography, and viewing range; (b) path length of the volcanic cone; (c) muon counts N_i^{obs}; (d) density ρ_i. The maximum value of the color bar indicates a density of >2.5 × 10^3 kg m^{-3} and the minimum value is <0.5 × 10^3 kg m^{-3}. (e) Density error $\Delta\rho = \left(\rho_i^{up} - \rho_i^{low}\right)/2$. The maximum value of the color bar indicates a density error of >0.25 × 10^3 kg m^{-3}.

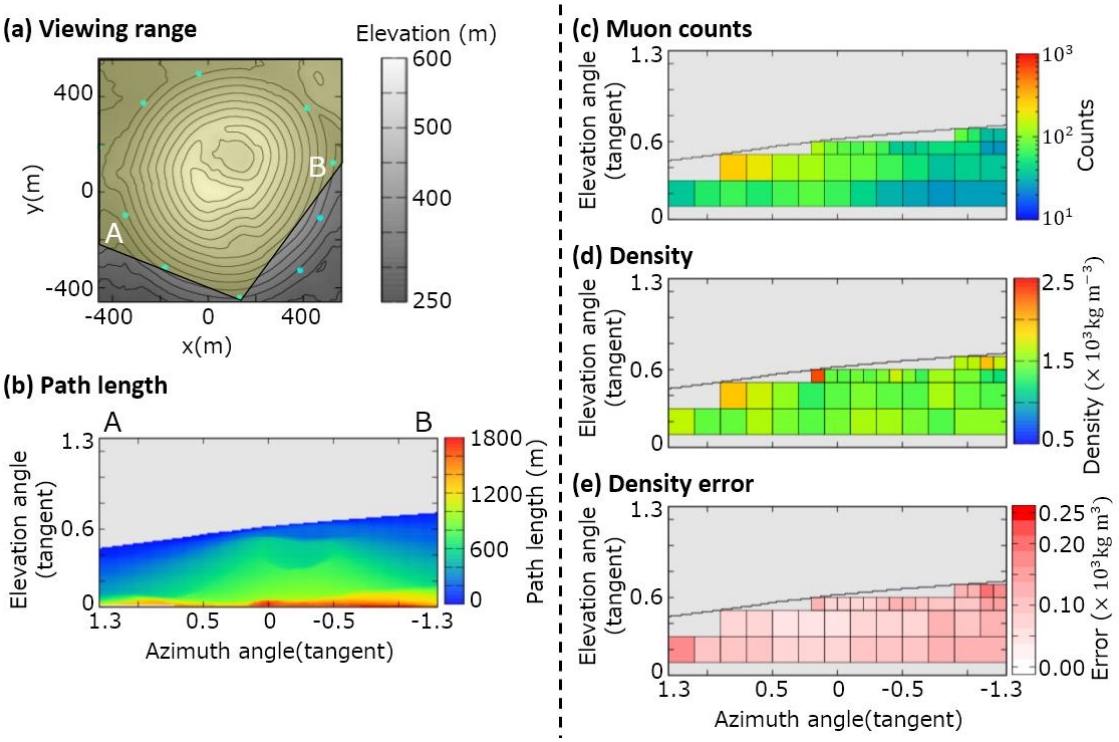

Figure B5. Observation site S. (a) Map, topography, and viewing range; (b) path length of the volcanic cone; (c) muon counts N_i^{obs}; (d) density ρ_i. The maximum value of the color bar indicates a density of >2.5 × 10^3 kg m^{-3} and the minimum value is <0.5 × 10^3 kg m^{-3}. (e) Density error $\Delta\rho = \left(\rho_i^{up} - \rho_i^{low}\right)/2$. The maximum value of the color bar indicates a density error of >0.25 × 10^3 kg m^{-3}.

905

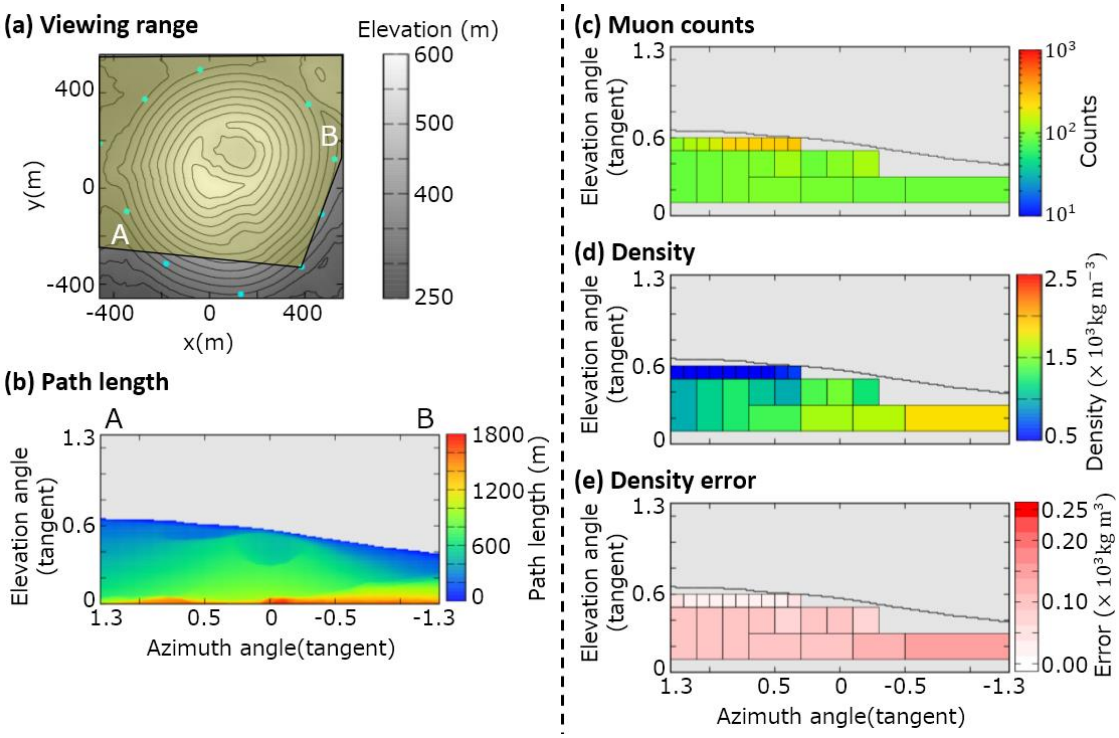

906

907

908 Figure B6. Observation site SE. (a) Map, topography, and viewing range; (b) path

909 length of the volcanic cone; (c) muon counts N_i^{obs}; (d) density ρ_i. The maximum value of

910 the color bar indicates a density of >2.5 × 10^3 kg m^{-3} and the minimum value is <0.5

911 × 10^3 kg m^{-3}. (e) Density error $\Delta\rho = \left(\rho_i^{up} - \rho_i^{low}\right)/2$. The maximum value of the color

912 bar indicates a density error of >0.25 × 10^3 kg m^{-3}.

913

914

915

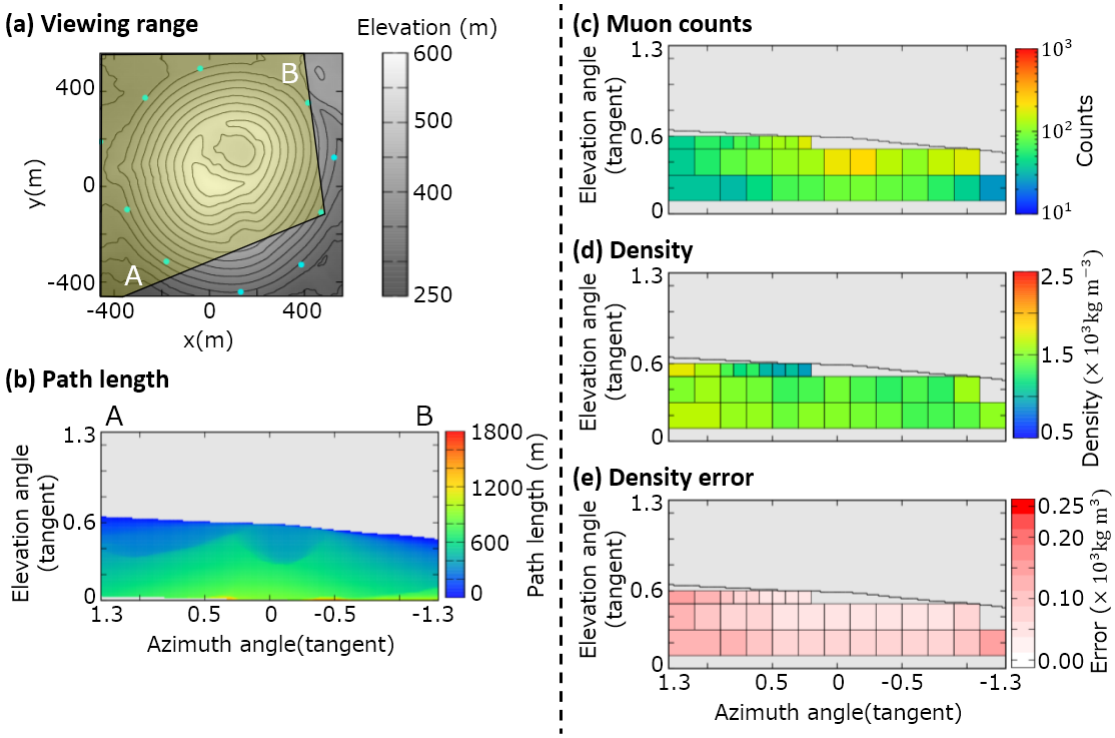

Figure B7. Observation site ESE. (a) Map, topography, and viewing range; (b) path length of the volcanic cone; (c) muon counts N_i^{obs}; (d) density ρ_i. The maximum value of the color bar indicates a density of >2.5 × 10^3 kg m^{-3} and the minimum value is <0.5 × 10^3 kg m^{-3}. (e) Density error $\Delta\rho = \left(\rho_i^{up} - \rho_i^{low}\right)/2$. The maximum value of the color bar indicates a density error of >0.25 × 10^3 kg m^{-3}.

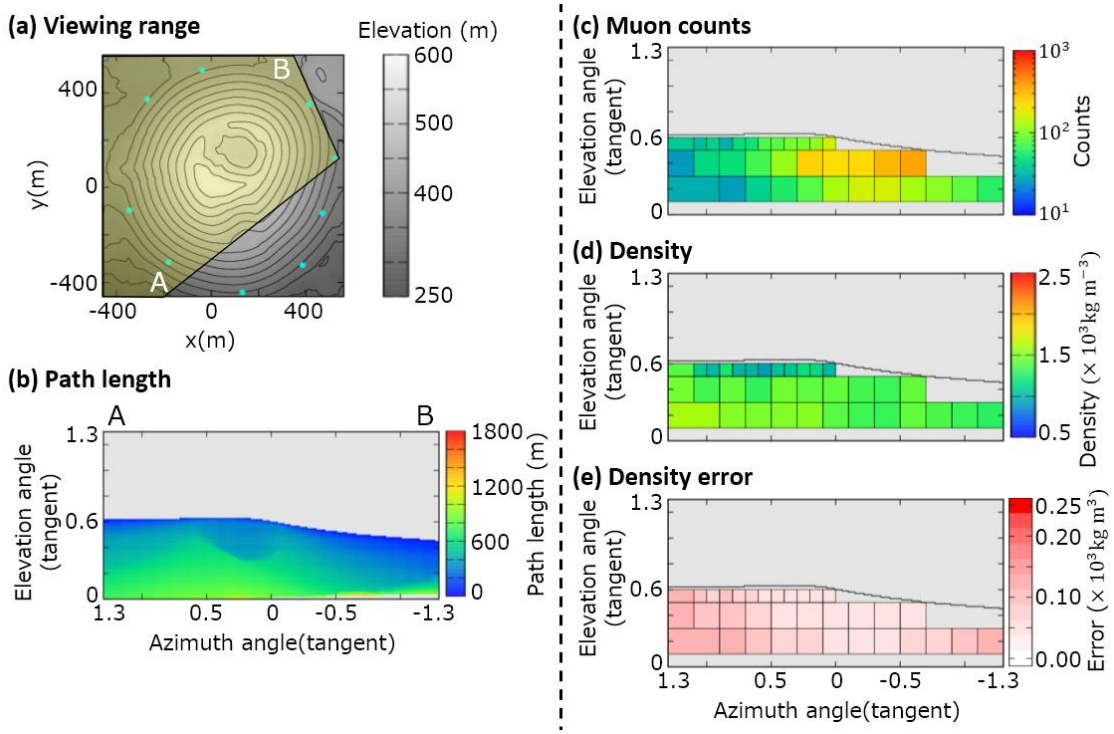

Figure B8. Observation site E. (a) Map, topography, and viewing range; (b) path length of the volcanic cone; (c) muon counts N_i^{obs}; (d) density ρ_i. The maximum value of the color bar indicates a density of >2.5 × 10^3 kg m^{-3} and the minimum value is <0.5 × 10^3 kg m^{-3}. (e) Density error $\Delta\rho = \left(\rho_i^{up} - \rho_i^{low}\right)/2$. The maximum value of the color bar indicates a density error of >0.25 × 10^3 kg m^{-3}.

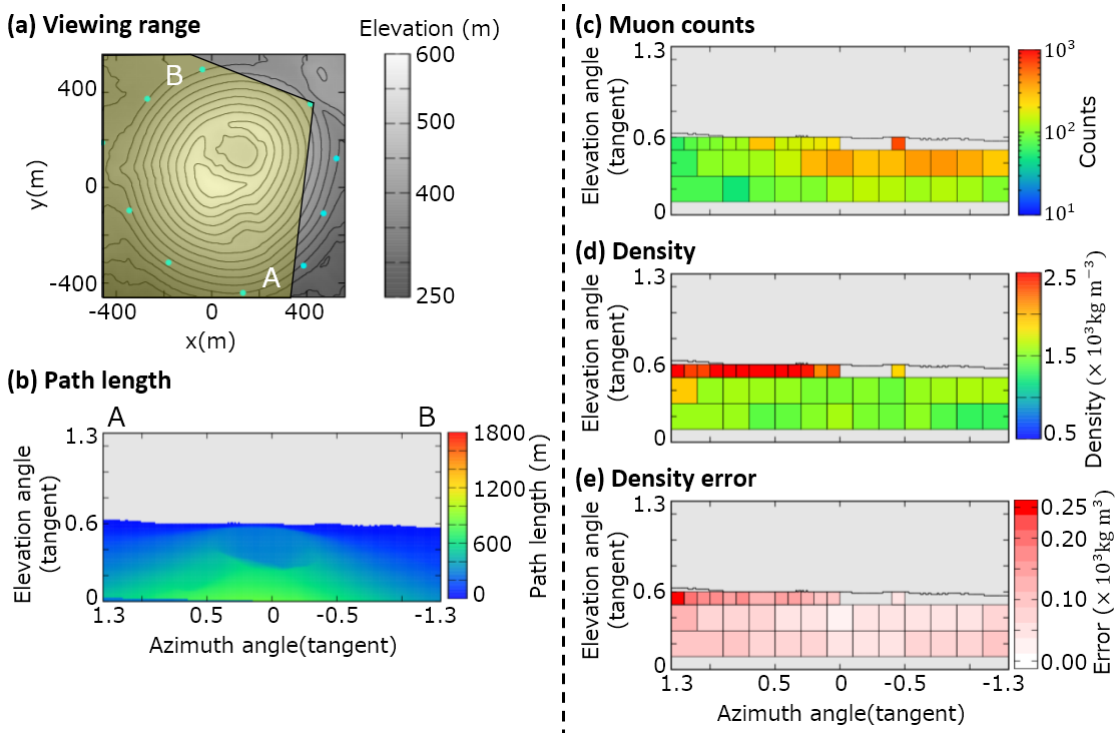

Figure B9. Observation site NE. (a) Map, topography, and viewing range; (b) path length of the volcanic cone; (c) muon counts N_i^{obs}; (d) density ρ_i. The maximum value of the color bar indicates a density of >2.5 × 10^3 kg m^{-3} and the minimum value is <0.5 × 10^3 kg m^{-3}. (e) Density error $\Delta\rho = \left(\rho_i^{up} - \rho_i^{low}\right)/2$. The maximum value of the color bar indicates a density error of >0.25 × 10^3 kg m^{-3}.

947

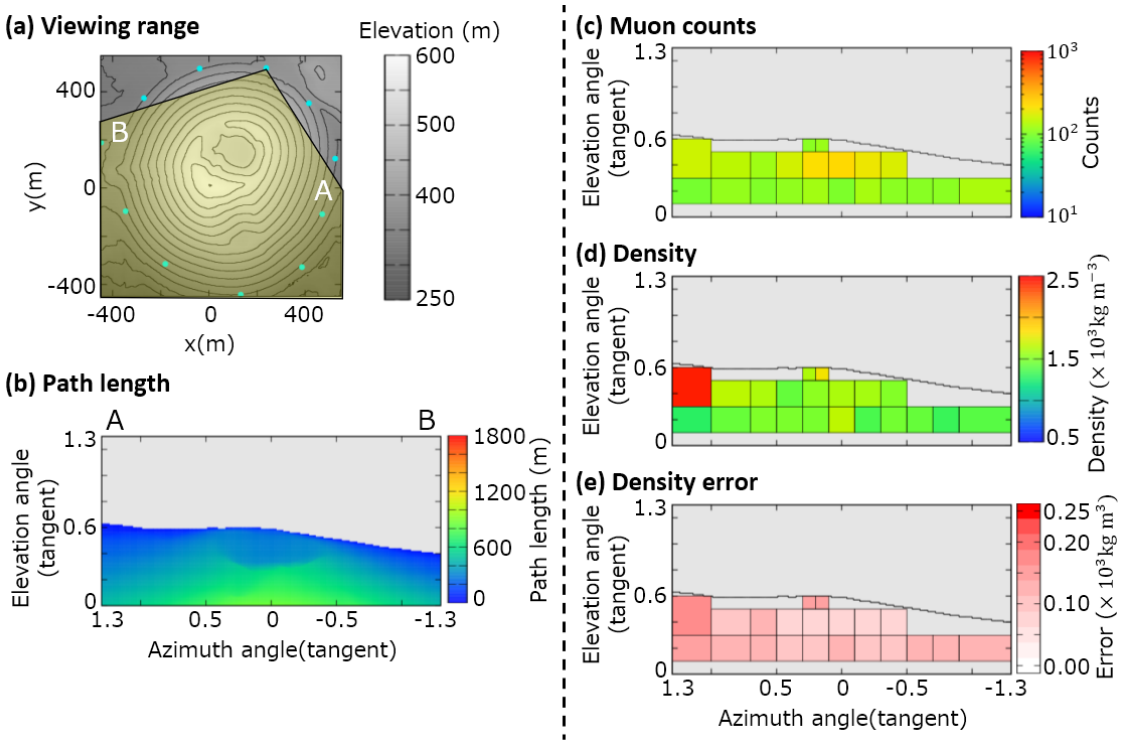

948

949

950 Figure B10. Observation site NNE. (a) Map, topography, and viewing range; (b) path

951 length of the volcanic cone; (c) muon counts N_i^{obs}; (d) density ρ_i. The maximum value of

952 the color bar indicates a density of >2.5 × 10^3 kg m^{-3} and the minimum value is <0.5

953 × 10^3 kg m^{-3}. (e) Density error $\Delta\rho = \left(\rho_i^{up} - \rho_i^{low}\right)/2$. The maximum value of the color

954 bar indicates a density error of >0.25 × 10^3 kg m^{-3}.

955

956

Code availability

Participants of this study did not agree for their code to be shared publicly, so supporting code is not available.

Data availability

The data of this study are available from the corresponding author upon reasonable request.

Author contribution

Miyamoto, Nagahara, Koyama, and Suzuki discussed the significance of this study and were involved in study design. Morishima checked the quality of nuclear emulsion, produced the films, and prepared the developing solution. Miyamoto and Nagahara designed the new emulsion film detector, installed the detectors, and developed the films after the muon exposure. Nakano operated the automated track readout system for the scanning of films. Miyamoto and Nagahara analyzed the track data and determine the density values. All of authors considered the results of this study.

Competing interests

The authors have no conflicts of interest directly relevant to the content of this article.